Superconductivity 9 (2024) 100073

Contents lists available at ScienceDirect

Superconductivity

journal homepage: www.elsevier.com/locate/supcon

Review

Review of Moiré superconductivity and application of the Roeser-Huber formula

Michael R. Koblischka *, Anjela Koblischka-Veneva

Institute of Experimental Physics, Saarland University, Campus C 6 3, 66123 Saarbrücken, Germany

ARTICLE INFO

Keywords:
Moiré Superconductors
Twisted bilayer graphene
Magic angle
Multilayer graphene stacks
Superconducting transition temperature
Roeser-Huber formalism

ABSTRACT

Moiré superconductivity represents a new class of superconducting materials since the discovery of superconductivity in magic-angle (1.1°) twisted bi-layer graphene (MATBG), forming a Moiré lattice with a much bigger crystal parameter as the original lattice constant of graphene. Hence, experimentally changing the Moiré twist angle, $0.93^{\circ} \leqslant \Theta \leqslant 1.27$, leads to a variation of the superconducting properties and enables a new way of engineering 2D superconducting materials. Details of the robust superconducting state of MATBG as function of charge carrier density, temperature and applied magnetic fields are reviewed. The influence of the top/bottom hexagonal boron nitride layer thickness on the superconducting properties of MATBG was also demonstrated in the literature. In all fabricated MATBG devices, changing of the charge carrier density leads to the appearance of insulating, metallic and even ferromagnetic states, which separate several superconducting domes in the phase diagram (longitudinal resistance, R_{xx}, as function of temperature T and charge carrier density, n). Further works have considered MATBG combined with WSe_2-layers, twisted bi-layer WSe_2, magic-angle tri-layer graphene (MATTG), and most recently, four-layer (MAT4G) and five-layer (MAT5G) stacks. The differences between the layered, cuprate high-T_c superconductors and the Moiré superconductors are compiled together. The collected information is then used to apply the Roeser-Huber formalism to Moiré-type superconductivity to calculate the superconducting transition temperature, T_c, using only information of the Moiré lattice and the electronic configuration. To account for the different charge carrier densities in the experimental data sets and the low charge carrier mass demands that a new parameter η must be introduced to the Roeser-Huber formalism to enable the description of several superconducting domes found in the phase diagram for a given Moiré angle. Doing so, the calculated data fit well to the correlation curve defined within the Roeser-Huber formalism.

Contents

* Corresponding author.
E-mail addresses: m.koblischka@ieee.org (M.R. Koblischka), a.koblischka@gmail.com (A. Koblischka-Veneva).

https://doi.org/10.1016/j.supcon.2023.100073
Available online 22 November 20232772-8307/

1. Introduction

Moiré superconductivity, which was first demonstrated experimentally in 2018, involves creating large, periodic superstructures in 2D materials as compared to the atomic scale. The first sample belonging to this new family of superconductors was found when stacking two graphene layers together with a small misalignment angle, $\Theta \sim 1.1^\circ$, called also the magic angle [1,2]. This graphene stack is called magic-angle twisted bilayer graphene (abbreviated MATBG or tBLG, which may describe also other twist angles as the magic ones) [2,3]. The misalignment between the two graphene layers creates a Moiré pattern which has a spatial period, a_M, being a factor $1/\Theta$ larger than the unit cell on the atomic level. At the so-called magic angles, the Fermi velocity drops to zero, and the first magic angle is predicted to be $\Theta_{magic} \approx 1.1^\circ$. Near this twist angle, the energy bands near charge neutrality, which are separated from other bands by single-particle gaps, become remarkably flat [4,5]. The typical energy scale for the entire bandwidth is about 5–10 meV. Experiments enabled the flatness of these bands to be confirmed by an high effective mass seen in quantum oscillations, and correlated insulating states at half-filling of these bands were observed [1], corresponding to $n = \pm n_s/2$ with $n = C \cdot V_g/e_0$ being the charge carrier density defined by the applied gate voltage V_g, C corresponds to the gate capacitance per unit area, and e_0 is the electron charge. Electrostatic doping the material away from these correlated insulating states enabled the observation of tunable zero-resistance states, which correspond to the presence of superconductivity. Very remarkably, the superconducting onset temperatures reported in the literature can be several degrees K high.

Since these first experimental reports, superconductivity in MATBG has been observed in ambient conditions [6–10] and under pressure [3] by other authors in the literature as well, including various twist angles around the magic angle, various charge carrier densities, and different thicknesses of the hexagonal boron nitride (abbreviated h-BN) layers on top and bottom of the MATBG [10]. The superconducting properties, including the critical fields and the superconducting parameters κ, λ_L and ξ of these samples, are well documented including a classification of the Moiré superconductors as presented by Talantsev [11].

Furthermore, the superconductivity of a trilayer stack (MATTG) of graphene was reported [12,13], in an ABC-type trilayer stack [14], and recently, the stacking was extended to four twisted graphene layers (MAT4G) and even 5 layers (MAT5G) with alternate angles ($\pm\Theta$) [15–17]. Arora et al. have combined MATBG with a monolayer of WSe_2 additional to the h-BN layers [18]. The basic idea of Moiré superconductivity was further extended in a report of superconductivity in misaligned (Θ = 1°, 4°) double layers of WSe_2 [19], but the data provided concerning the superconducting properties of this system are much less convincing as compared to the other reports on MATBG as mentioned also in another review [20]. Similar detailed experiments concerning superconductivity on other types of twisted, bi-layered hexagonal lattice materials like stanene or borophene are still missing in the literature [21,22].

The appearance of several superconducting domes in the phase diagram (here, the longitudinal resistivity is plotted color-coded as a function of temperature, $R_{xx}(T)$ as function of charge carrier density n) was described first by Lu et al. [6]. These superconducting domes, being quite similar to the doping diagram of the cuprate HTSc, are separated by metallic states, insulators and even ferromagnets. Thus, this topic is intensively investigated by band structure calculations [23–28] and gives rise to a continuously growing number of new experimental and theoretical aspects [29–54].

It is important to note here that Moiré patterns can be formed also in cases when different types of 2D-layered materials are stacked together, with or without angular misalignment, or between a 2D layer and a substrate [55,56]. As result, the resulting Moiré lattice parameter, a_M, may be considerably larger than the original atomic unit cells of any ingredient. Several details of the mathematics of Moiré patterns were already presented in Refs. [57–60]. Thus, the stacking of various 2D-layered materials offers a versatile new way to control superconductivity in layered 2D-systems ("Moiré superconductors"), the full potential of which has been barely explored yet [61,62,17,63,16,64–66]. So, to further investigate this field and unleash more possibilities to find new materials with higher T_c's, a relatively simple calculation procedure which can be included in machine-learning approaches, see, e.g., Refs. [67–72], is extremely useful.

As the lattice constant of the Moiré pattern plays an important role for the observation of superconductivity, it is straightforward to follow this relation between superconductivity and the characteristic sample dimension in more detail. For cuprate high-temperature superconductors (HTSc), and later also for iron-based superconductors (IBS), fullerenes, elemental superconductors and metallic alloys, the Roeser-Huber fomula was developed to calculate the superconducting transition temperature, T_c. This approach only requires to find a characteristic length of the sample crystallography, x, and some knowledge about the electronic configuration [73–81]. All this information may be found in existing databases. Using the Roeser-Huber formalism, the T_c of several superconducting materials could be calculated with only a small error margin [79,81], and recently, the approach was even employed to predict T_c of metallic hydrogen with different crystal lattices [82]. In case of double-doped, cuprate HTSc materials (e.g., the Cu–O-planes of $Bi_2Sr_2CaCu_2O_{8+\delta}$ (Bi-2212) doped by oxygen and by additional metal ions like Y or La), two characteristic doping patterns result, and the final T_c of the material is calculated as a Moiré-pattern of the two doping arrangements [75]. Thus, it is only straightforward to apply this calculation scheme to the real Moiré superconductors, where a clear crystallographic relation is defined by the orientation of the MATBG and by the unit cell of the MATBG itself.

In the present contribution, the existing literature concerning the superconducting properties with special emphasis on the transition temperatures of the various Moiré superconductors are reviewed, and the application of the Roeser-Huber formalism to Moiré superconductivity is presented including the introduction of a new parameter to account for the variations in charge carrier density.

This paper is organized as follows: In Section 2, some details of the fabrication steps of the MATBG samples are outlined and the resistance measurements performed to observe superconductivity in several superconducting domes are presented. Section 3 discusses the properties of the superconducting phase diagrams of the various Moiré superconductors presented in the literature. Then, in Section 4 the Roeser-Huber formalism as developed for HTSc is introduced. Section 5 discusses the calculation of the superconducting transition temperatures of the Moiré superconductors solely on the base of the electronic configuration and the respective Moiré parameters. Finally, Section 6 gives some conclusions and an outlook for future developments.

2. Materials and methods

2.1. Moiré superlattices

Fig. 1a presents a Moiré superlattice of two graphene layers (blue, red) twisted by an angle of 5° for clarity. The resulting lattice parameter, a_M (sometimes also denoted Moiré wavelength, λ), is indicated by a black line. In Ref. [12], also a tri-layer structure was presented with the top and bottom layers tilted by ±5° with respect to the center layer. This situation is depicted in Fig. 1b.

The lattice parameter of graphene is a_0^G = 0.246 nm, and the one of WSe_2 is $a_0^{WSe_2}$ = 0.353 nm [83]. Then, the possible Moiré patterns of two identical layers at an angle Θ have a periodicity according to

$$a_M = \frac{a_0}{2 \cdot \sin(\Theta/2)} \quad . \tag{1}$$

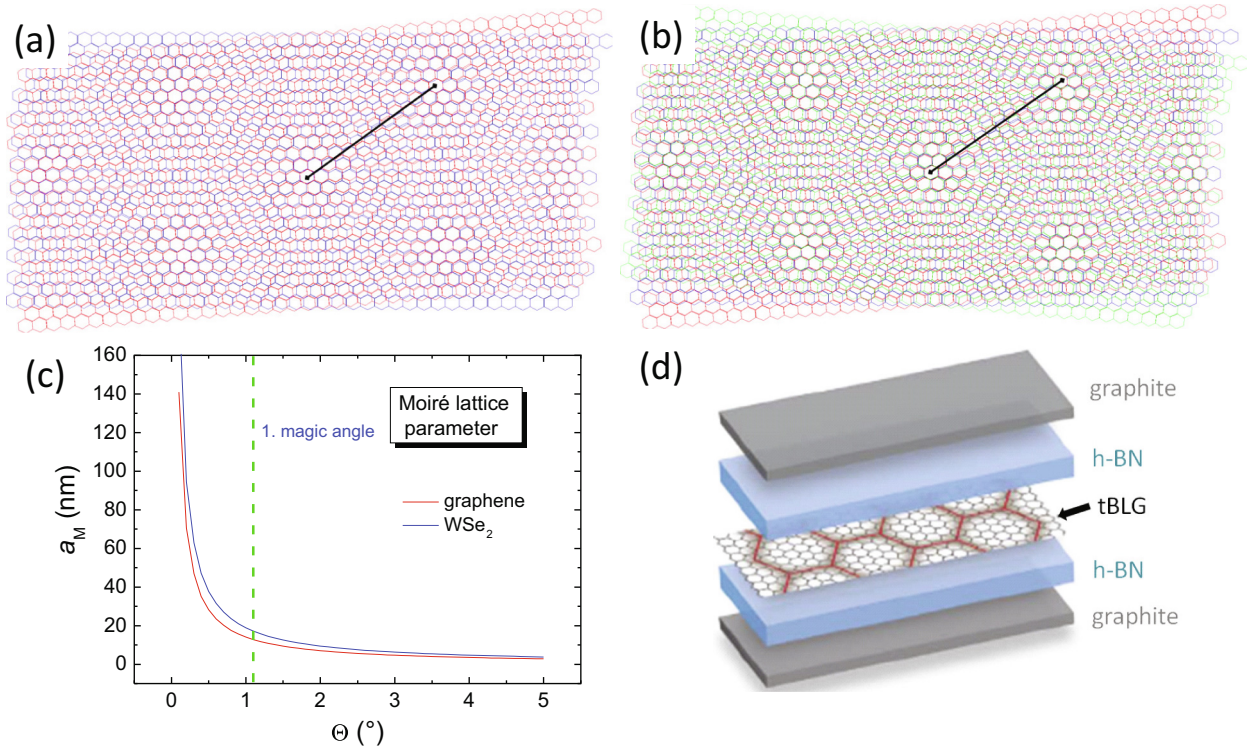

Fig. 1. (a) Moiré pattern of two graphene layers (red, blue) tilted by 5°. This value was chosen for clarity. The black line indicates the resulting Moiré lattice parameter, a_M. (b) Moiré pattern of a tri-layer graphene system (red, blue, green) with the top and bottom layer tilted by ±5° with respect to the center layer. (c) Moiré lattice parameter, a_M, of two twisted graphene as function of the twist angle, Θ. The first magic angle, 1.1°, is marked by a dashed green line (- - - -). (d) Schematic view of the various layers in a device for resistance measurement. Figure adapted from Ref. [3]. (For interpretation of the references to colour in this figure legend, the reader is referred to the web version of this article.)

Fig. 1c depicts the dependence of the Moiré lattice constant, a_M, on the twist angle Θ for graphene as well as for WSe_2.

The magic angle Θ_{magic} is given by [85]

$$\Theta_{magic} = \arccos\left(\frac{k^2 + 4kl + l^2}{2 \cdot (k^2 + kl + l^2)}\right) \quad , \tag{2}$$

with k, l being integers. The first magic angle, 1.1°, is indicated in Fig. 1c by a dashed green line.

The accuracy achieved to determine the tilt angle of the graphene layers is typically ~0.03° [10]; Stepanov et al. describe the twist homogeneity within a device as good as 0.01° per 10 μm [9]. Thus, the twist angles in MATBG are well defined with only small experimental error. This will be an important issue for the T_c-calculations with the Roeser-Huber formalism as shown in Section 4 below.

It has been theoretically shown [84] that for three or more twisted layers of graphene, there are similar series of 'magic' angles if the layers are alternatively twisted by $(\Theta, -\Theta, \Theta, \ldots)$ (Fig. 2a). As illustrated in Fig. 2b, they are in fact related by simple trigonometric transforma-

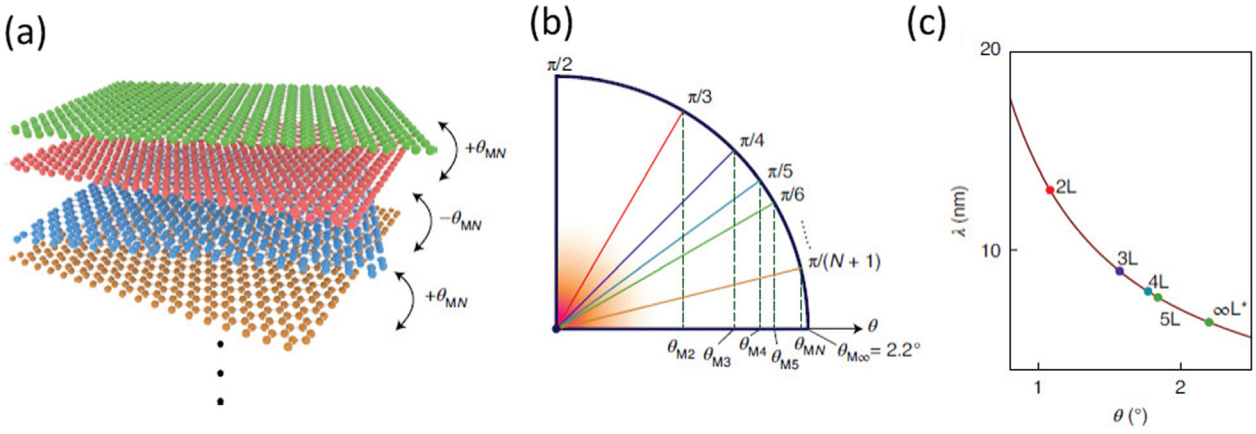

Fig. 2. (a) Twisted multilayer graphene with alternating twist angles Θ_{MN} and $-\Theta_{MN}$ between the adjacent layers, where Θ_{MN} denotes the magic angle Θ_M specific to a N-layer structure. (b) In the chiral limit, Θ_M can be obtained for any N from the asymptotic value $\Theta_{M\infty} = 2.2°$, by a simple trigonometric transformation. (c) Dependence of a_M on the twist angle. Note that only structures with atomic alignment between the nth and $(n+2)$th layers (L) are considered here, so that a single distance a_M or wavelength λ can be defined according to Ref. [84].

tions, that is, the largest magic angle can be expressed as $\Theta_N = \Theta_\infty \cos\frac{\pi}{N+1}$, where N is the number of layers and $\Theta_\infty = 2\Theta_{N=2}$ is the asymptotic limit of the largest magic angle as $N \to \infty$. As N increases, the magic angle increases and a_M decreases. Fig. 2c gives the dependence of a_M on the twist angle. Using this principle, high-quality, twisted magic-angle tetralayer and pentalayer graphene devices (MAT4G and MAT5G, respectively) were fabricated and measured by two independent groups [16,17].

Here, it is important to mention that all the results obtained on graphene-based Moiré superconductors stem from manually assembled stacks of monolayer graphene. This involves, of course, multiple complicated operations, and thus the resulting devices are small and difficult to be exactly reproduced. This situation is, e.g., obvious from the measurements of Saito et al. [10] as shown in Fig. 4 below. Thus, to achieve a higher reproduction rate and larger devices which could be used for electronic applications, different production routes are required. This was addressed in a recent review by Cai and Yu [86]. The current production methods of tBLG comprise chemical vapor deposition (CVD) on metal catalysts [87], epitaxial growth on SiC substrate [88], folding monolayer graphene [89] and stacking monolayer graphene [90]. These methods can be divided into two main categories: the direct growth approaches and manual assembly [86]. These completely different preparation processes show distinctive advantages and disadvantages, however, the precise control over the twist angles and super-clean interfaces are the ultimate demands for any preparation method applied for the fabrication of tBLG devices. As result, the progress achieved in the fabrication of tBLG is much slower than monolayer graphene due to the required precise control over twisted structures. The demands for super-clean interfaces, which directly affect the physical properties and application of tBLG, excludes the use of organic polymers. Thus, further advancing the preparation methods for tBLG is the main challenge for future development. In particular, the direct growth of high-quality and super-clean tBLG with various twist angles will have a great practical significance for twistronics.

2.2. Devices and resistance measurements

The superlattice density $n_s = 4/A$ was defined to be the density that corresponds to full-filling each set of degenerate superlattice bands, where $A \approx \sqrt{3}a^2/(2\Theta^2)$ is the area of the Moiré unit cell (a = 0.246 nm is the lattice constant of the underlying graphene lattice) and Θ is the twist angle. The resulting electron density is $n_0 = A_0^{-1} \approx 10^{12}$ cm^{-2}, where A_0 is the area of the Moiré unit cell. Correlated states were observed by various authors at all integer fillings of $\nu = n/n_0$ (where n denotes the gate-modulated carrier density) at Moiré band filling factors $\nu = 0, \pm1, \pm2, \pm\ldots$

To measure the superconducting properties of MATBG by means of resistance measurements, a structure called device is fabricated using the tear-and-stack or cut-and-stack method encapsulating the MATBG

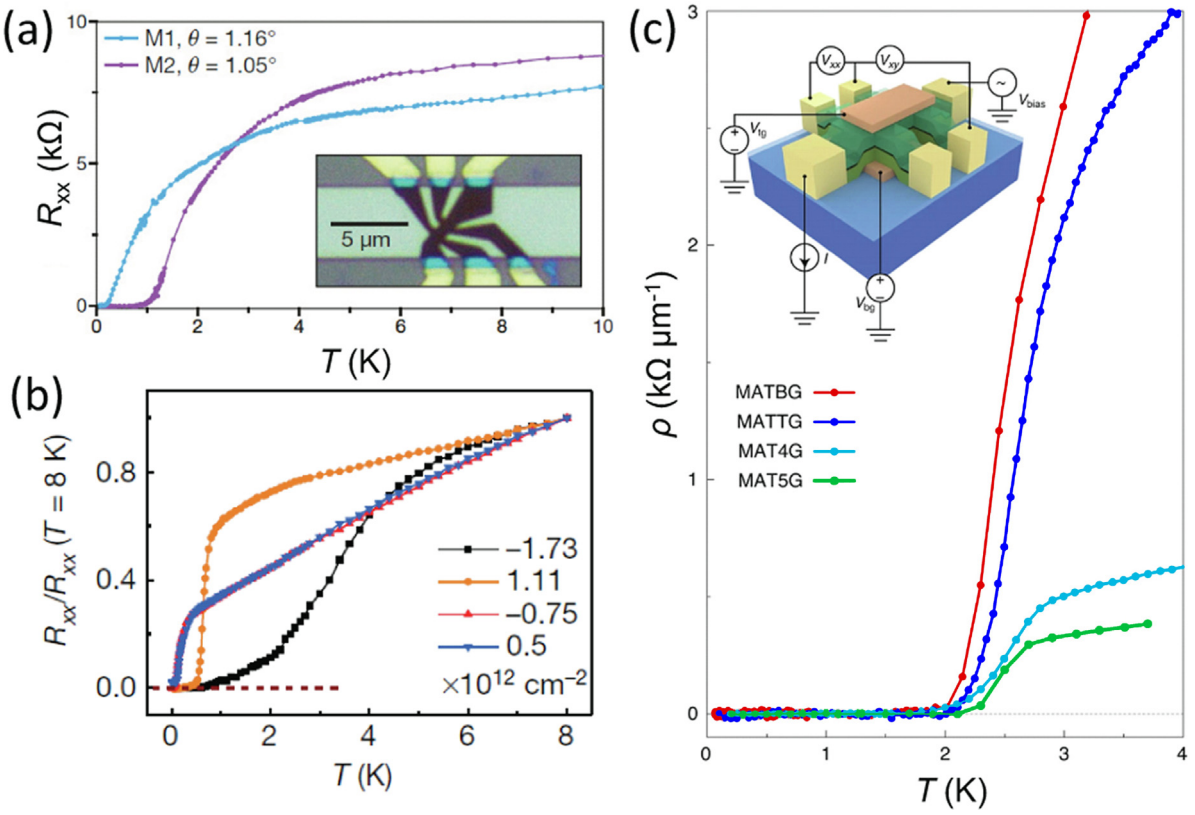

Fig. 3. (a) Longitudinal resistance, R_{xx}, being in the kΩ-regime, measured by four-probe method in two devices M1 and M2 with twist angles of $\Theta = 1.16°$ and $\Theta = 1.05°$, respectively. The inset shows an optical image of device M1, including the main 'Hall' bar (dark brown), the electrical contacts (gold), the back gate (light green) and the SiO_2/Si substrate (dark grey). Reproduced with permission from Ref. [2]. (b) Longitudinal resistance at optimal doping of various superconducting domes at different charge carrier densities, n_s, as a function of temperature (see also Fig. 4). The resistance is normalized to its value at 8 K. Note that data points for $n = -7.5 \times 10^{11}$ cm^{-2} are overlaid by the data points for $n = 5 \times 10^{11}$ cm^{-2}, as both curves follow a very similar line. Reproduced with permission from Ref. [6]. (c) Graph of the resistivity ρ versus T for MATBG (—●—, filling factor $\nu = -2.32$), MATTG (—●—, $\nu = -2.4$ and electric displacement field $D/\varepsilon_0 = -0.44$ V nm^{-1}), MAT4G (—●—, $\nu = 2.37$ and $D/\varepsilon_0 = -0.32$ V nm^{-1}) and MAT5G (—●—, $\nu = 3.05$ and $D/\varepsilon_0 = 0.23$ V nm^{-1}) (i.e., $N = 2, 3, 4, 5$), showing superconducting transitions in all four systems at their respective magic angle. Note here that the measured resistivity decreases on increasing N. The inset shows a schematic view of the devices employed. Reproduced with permission from Ref. [16].

between h-BN layers. This arrangement is then patterned into a Hall bar geometry with multiple leads using electron beam lithography and reactive ion-etching. The final device is placed on a Si/SiO_2 substrate with an intermediate thick graphite layer serving as back gate. Another graphite layer on top serves for protection. This construction is required to prepare proper electric contacts to the sample. A schematic drawing of the arrangement of the various layers is given in Fig. 1d as well as in the inset to Fig. 3c and a device ready for measurement is given as an inset to Fig. 3a. As mentioned before, only small devices with low reproducibility can be prepared in this way.

Fig. 3a and b present typical four-point resistance measurements as a function of temperature for MATBG samples. In Fig. 3a, the measured resistance, R_{xx} is presented for two twist angles, 1.16° (M1) and 1.05° (M2) [2]. The inset shows the arrangement of sample and electric contacts ready for measurement. Fig. 3b gives similar data from Ref. [6], but only for one angle (1.10°) and normalized to the resistance measured at 8 K. The different curves are obtained for various charge carrier densities, ranging between $+1.11 \times 10^{12}$ cm^{-2} to -1.73×10^{12} cm^{-2}. From this plot, it is obvious that the shape of the curves as well as the determined transition temperatures strongly vary with the charge carrier density. The variation of the charge carrier densities in the devices is achieved by tuning the gate voltage (V_{gate}), which enables an extensive study of the phase diagram of all types of tBLG devices.

The measured longitudinal resistances, R_{xx}, in the normal state for MATBG devices are in the range 10 kΩ…20 kΩ, which is quite high for such small-sized devices. As result, the superconducting transition temperature determined by 50% of the normal-state resistivity, ρ_n, criterion is still around 2.5 kΩ. Fig. 3c presents the evolution of the resistivity with the number of layers as measured by Park et al. [16]. From this diagram, it is obvious that resistance/resistivity decreases on increasing N, but still stays in the low kΩ-regime. Thus, a true superconducting state with zero resistance could not yet be documented in any of the experiments carried out in the literature. It is important to note here that the change in resistance by 10–15 times within some temperature range does not guarantee that this is a true superconducting transition [92], as it was again demonstrated recently for LK-99 case [93]. However, in the following we will use the T_c-data for the Moiré superconductors as mentioned in the literature and also formally apply the 50% transition analysis to the published data.

3. Phase diagrams of Moiré superconductors and comparison with cuprate HTSc materials

At $\nu \approx -2$, superconductivity was observed in MATBG devices M1 and M2 below critical temperatures of up to 3 K [2]. Figs. 4a and b present sections of the phase diagram for negative charge carrier densities for the samples M1 ($\Theta = 1.16°$) and M2 ($\Theta = 1.05°$). Here, the $R_{xx}(T)$-curves are plotted as vertical lines indicated by the green dashed line in (b), using color coding for R_{xx}) as function of the charge carrier density. The dashed white lines are defined as 50% resistance to the normal state. Here, we see that the borders of the superconducting domes are not sharp and varying with n, thus leading to a large variation of the superconducting transitions concerning T_c as well as the transition width, δT_c. These diagrams reveal that the twist angle a_M sets the possibility to observe superconductivity, but the resulting superconducting properties of the MATBG samples clearly depend on the charge carrier density.

In subseqent papers, a further variation of the charge carrier density revealed a complete sequence of insulating states, magnetic states as well as superconducting states. Such a full phase diagram is shown in Fig. 5a, reproduced from Ref. [6] on a MATBG sample with $\alpha = 1.1°$ (see also Table 2 below), presents the complete sequence of superconducting domes (SC), metallic behavior and correlated states (CS) when tuning the gate voltage between $\pm 3 \times 10^{12}$ cm^{-2}. In this diagram, also three new superconducting domes at much lower temperatures were observed, close to the $\nu = 0$ and $\nu = \pm 1$ insulating states. The red and green arrows indicate the superconducting transitions observed by Cao et al. [2] and Yankowitz et al. [3]. Fig. 5b demonstrates the effect of perpendicular magnetic field $B^{\perp}$ on the SC pockets observed in device D1, presenting a 2D map of the recorded longitudinal resistance, R_{xx}, as a function of $B^{\perp}$ and the total charge carrier density,n, measured at a base temperature of 16 mK.

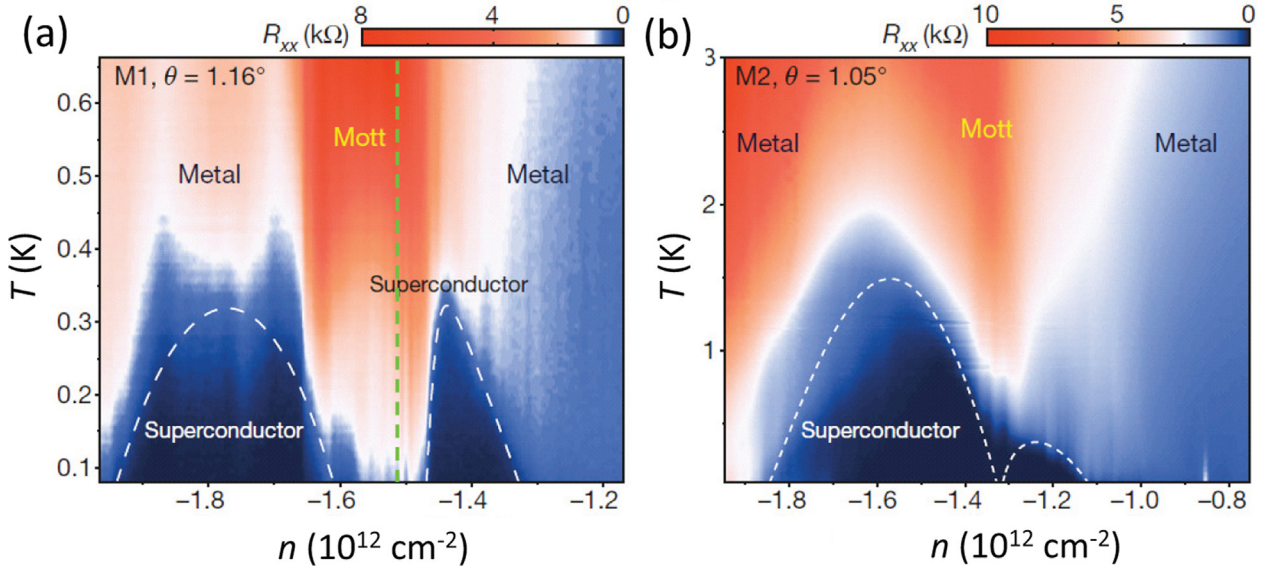

Fig. 4. (a). Four-probe resistance measurement on sample M1 ($\Theta = 1.16°$). The longitudinal resistance, R_{xx}, is measured at given charge carrier densities versus temperature, i.e., along the dashed-green lines and R_{xx} is represented via the color code, given above the diagram. Two superconducting domes (dark blue/black) are observed next to the half-filling state, which is labelled 'Mott' and centered around $-n_s/2 = -1.58 \times 10^{12}$ cm^{-2}. The remaining regions in the diagram are labelled as 'metal' owing to the metallic-like temperature dependence of R_{xx}. The highest critical temperature observed in device M1 is $T_c = 0.5$ K (at 50% of the normal-state resistance). (b), Same measurements as in (**a**), but for device M2, showing two asymmetric and overlapping domes. The highest critical temperature in this device is $T_c = 1.7$ K. Reproduced with permission from Ref. [2].

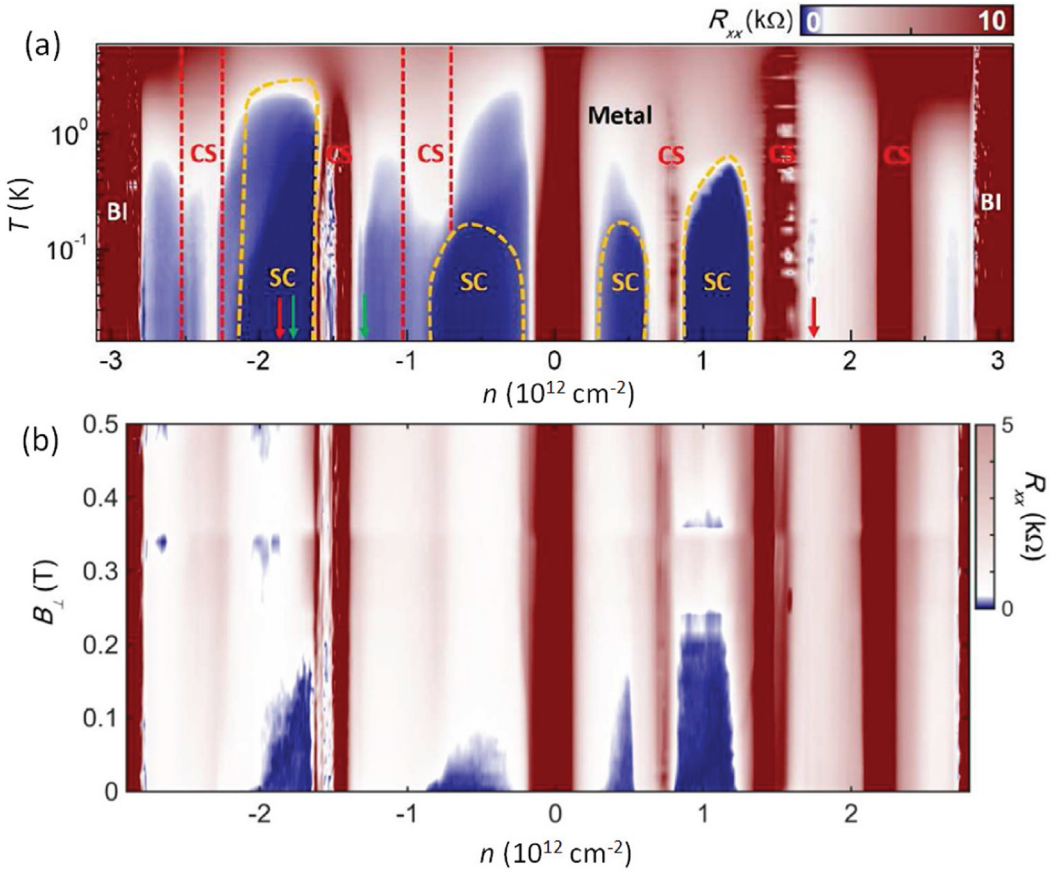

Fig. 5. (a) Color plot of longitudinal resistance versus charge carrier density and temperature of Ref. [6] on a MATBG sample with $\alpha = 1.1°$ (see also Table 2 below), showing different phases including metal, band insulator (BI), correlated state (CS) and superconducting state (SC). The boundaries of the superconducting domes – indicated by yellow lines – are defined by 50% resistance values relative to the normal state. Note that the transition from the metal to the superconducting state is not sharp at some carrier densities, which renders the proper determination of the value of T_c difficult. (b) 2D map of longitudinal resistance, R_{xx}, taken in applied magnetic fields, $B_\perp$, as function of the total charge carrier density, n at a temperature of 16 mK. Reproduced with permission from Ref. [6].

The phase diagram of MATBG, plotting temperature vs. charge carrier density is similar to that of the HTSc cuprates (where temperature is plotted vs. the doping level), and includes several dome-shaped regions corresponding to superconductivity. Furthermore, quantum oscillations in the longitudinal resistance of the material indicate the presence of small Fermi surfaces near the correlated insulating states, which is also the case in underdoped, cuprate HTSc. The small Fermi surface of MATBG, corresponding to a charge carrier density of about 10^{11} cm^2, and the relatively high resulting T_c's places the MATBG systems among the superconductors with the strongest pairing strength between electrons [2], which was later relativated by Talantsev [11] based on the thorough analysis of the available magnetic data.

As stated in [2], "one of the key advantages of this system is the in situ electrical tunability of the charge carrier density in a flat band with a bandwidth of the order of 10 meV". This enables the study of the phase diagram to be performed in unprecedented resolution on one given sample, avoiding the problems arising when studying various samples with different microstructures. However, there is also a drawback as the application of the gate voltage does not allow for magnetic measurements in magnetometers to be performed on these devices, so the most important hallmark of superconductivity, the Meissner effect [91,92], cannot be measured directly. For magneto-optic imaging [94,95] or for magnetic force microscopy (MFM) [96], the current MATBG devices are too small to enable proper measurements. One could imagine, however, to apply the scanning Hall probes [97,98], scanning SQUID [99] or the diamond color center [100,101] techniques to image the details of the magnetic states in MATBG, which were already predicted in a recent paper [102]. Nevertheless, other features of the superconducting state like the effect of applied magnetic fields on the superconducting transition, and the Fraunhofer patterns could be observed, which enabled a classification of the Moiré superconductors based on the magnetic data as presented by Talantsev [11].

An important experimental work was carried out by Saito et al. [10], demonstrating the effect of varying the thickness of the h-BN layer on the superconducting properties of tBLG, where $d_{\mathrm{h-BN}}$ varies between 6.7 nm and 68 nm for MATBG samples with different twist angles. In this work, the highest observed T_c-values for MATBG samples were reported. Figs. 6a–f present the influence of the h-BN cover layer thickness on the superconductivity of the MATBG devices 1 (a) – 5 (e) (Figs. 6a–e reproduced from Saito et al. [10]). The diagrams show the measured, color-coded R_{xx} as function of T and ν. For each device, the values of the twist angle Θ, its error margin and the thickness d of the h-BN layer are given. The dashed line in each image indicates the density $\nu = -2$. Fig. 6f gives a 3D-bar diagram of the highest T_c's recorded as function of d and Θ. Here, we can see directly that a thicker h-BN layer yields a higher value of T_c (see also the data collected in Table 2 below). The superconducting dome recorded for device 5 at $n = 1.79 \times 10^{12}$ cm^{-2} with $d = 45$ nm and α slightly above the magic angle yielding the highest T_c is the most robust one of sll devices investigated. However, we must note here that the increase of d does not change the charge carrier density in the MATBG. According to Saito et al. [10], the effect of increasing d is due to the

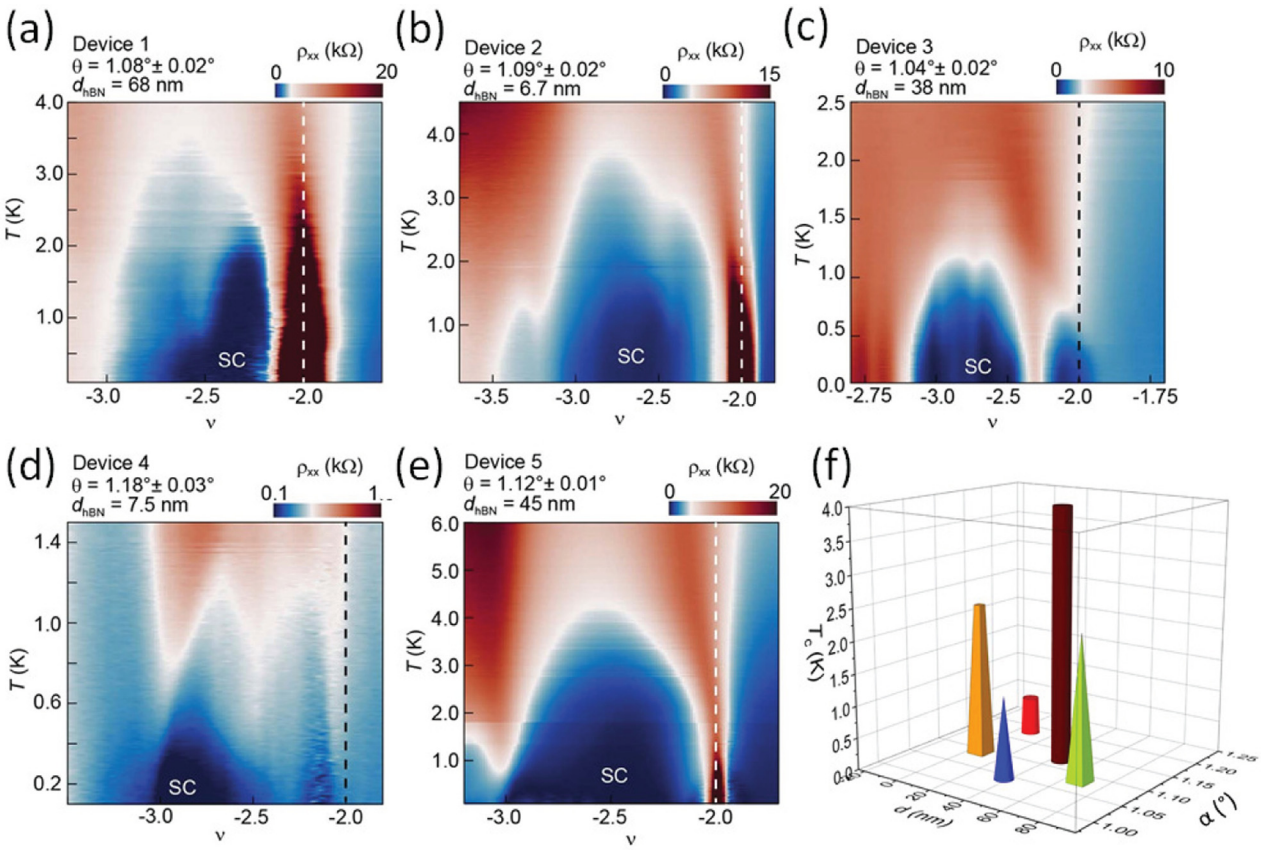

Fig. 6. Phase diagrams on tBLG revealing the influence of the h-BN layer thickness. The diagrams are presenting details of the 2D maps around a superconducting dome in each device [10] D1–D5. The white dashed lines show $\nu = -2$. (a) Device 1 ($\Theta = 1.08°, d_{\mathrm{h-BN}} = 68$ nm, ■). (b) Device 2 ($\Theta = 1.09°, d_{\mathrm{h-BN}} = 6.7$ nm, ■). (c) Device 3 ($\Theta = 1.04°, d_{\mathrm{h-BN}} = 38$ nm, ■). The superconducting phase is divided by a weak resistive state around $\nu = -2 - \delta$, which does not match the density of the state at $\nu = -2$, being estimated from the strong resistive states at $\nu = -4, 0, 2, 4$. (d) Device 4 ($\Theta = 1.18°, d_{\mathrm{h-BN}} = 7.5$ nm, ■). (e) Device 5 ($\Theta = 1.12°, d_{\mathrm{h-BN}} = 45$ nm, ■). Reproduced with permission from Ref. [10]. (f) 3D-bar diagram showing the highest values of T_c recorded in [10] as function of d and α. It is obvious from images (**a**), (**c**), (**e**) and (**f**) that thicker h-BN layers stabilize a strong and robust superconducting state with the highest T_c value of ~4 K recorded in (**e**).

separation of the channel from the gates, leading to varying degrees of screening of the Coulomb interaction. Furthermore, other experimentally not controllable parameters like the twist angles between h-BN and tBLG as well as strain may influence the measured T_c. Thus, the error bars shown in Fig. 8 below are quite large.

Figs. 7a,b present the $\nu - T$ phase diagrams for MAT4G and MAT5G by Park et al. [16], and Figs. 7c,d the results of Zhang et al. [17] on pentalayer graphene (MAT5G). Park et al. [16] found that the normal-state resistivity in MAT4G and MAT5G is considerably lower than that in MATBG and MATTG, which may be possibly due to the presence of extra highly dispersive Dirac bands, providing parallel conducting channels. As result, the observed range of filling factors in which superconductivity appears in MAT4G and MAT5G is generally wider as compared to MATBG and MATTG, starting close to $\nu = \pm 1$ and reaching beyond $\nu = \pm 3$. Superconductivity in MAT5G extends to or can even reach beyond $\nu = +4$. The authors conclude that considering that MATTG also had a wider superconducting dome as compared with MATBG [15,12], this observation suggests that increasing the number of layers could possibly increase the phase space robustness of the superconductivity. However, one should also note that for $N > 2$, ν does not indicate exclusively the filling factor of the flat bands, because some of the carriers induced by the gates fill also the dispersive bands.

Zhang et al. [17] showed not only the robust superconductivity for MAT5G (Fig. 7c), but also the effect of appyling a displacement field D on the resulting phase diagram as shown here in Fig. 7d.

Fig. 8a–c give various information on the superconducting state of MATBG (data collected by Lu et al. [6]) when applying an external magnetic field to the MATBG devices. The variation of the longitudinal resistance, $R_{xx}(T)$, is given in Fig. 9a for applied magnetic fields of 0, 130, 230 and 300 mT. As expected from a superconducting material, the onset of T_c reduces with the application of a magnetic field until the superconducting transition is completely suppressed in higher fields. Fig. 9b gives the resistance, R_{xx} (color-coded), as function of the perpendicularly applied magnetic field, $B_{\perp}$, for various charge carrier densities, n, at a temperature of 16 mK. This diagram directly shows the respective magnetic fields required to suppress superconductivity. Finally, Fig. 9c presents a Fraunhofer interference pattern measured in the superconducting state. This diagram plots the applied field, B, on the x-axis and the applied current, I, on the y-axis. The color code in this plot stands here for $\mathrm{d}V_{xx}/\mathrm{d}I$. This Fraunhofer pattern directly manifests the superconducting character, i.e., the dependence of the critical current on the external applied magnetic flux like in a Josephson junction, as a true measurement of the Meissner effect is not possible for a MATBG device. Figs. 9d–f present the analysis of Talantsev et al. concerning the superconduting parameters of MATBG samples. The superconducting parameters were derived from fits to the data of the upper critical field, $H_{c2}(T)$ and the critical current density, $J_c(T)$(self field), following the models by [103–111]. All this gives valuable information on the properties of the superconducting state(s) in MATBG samples.

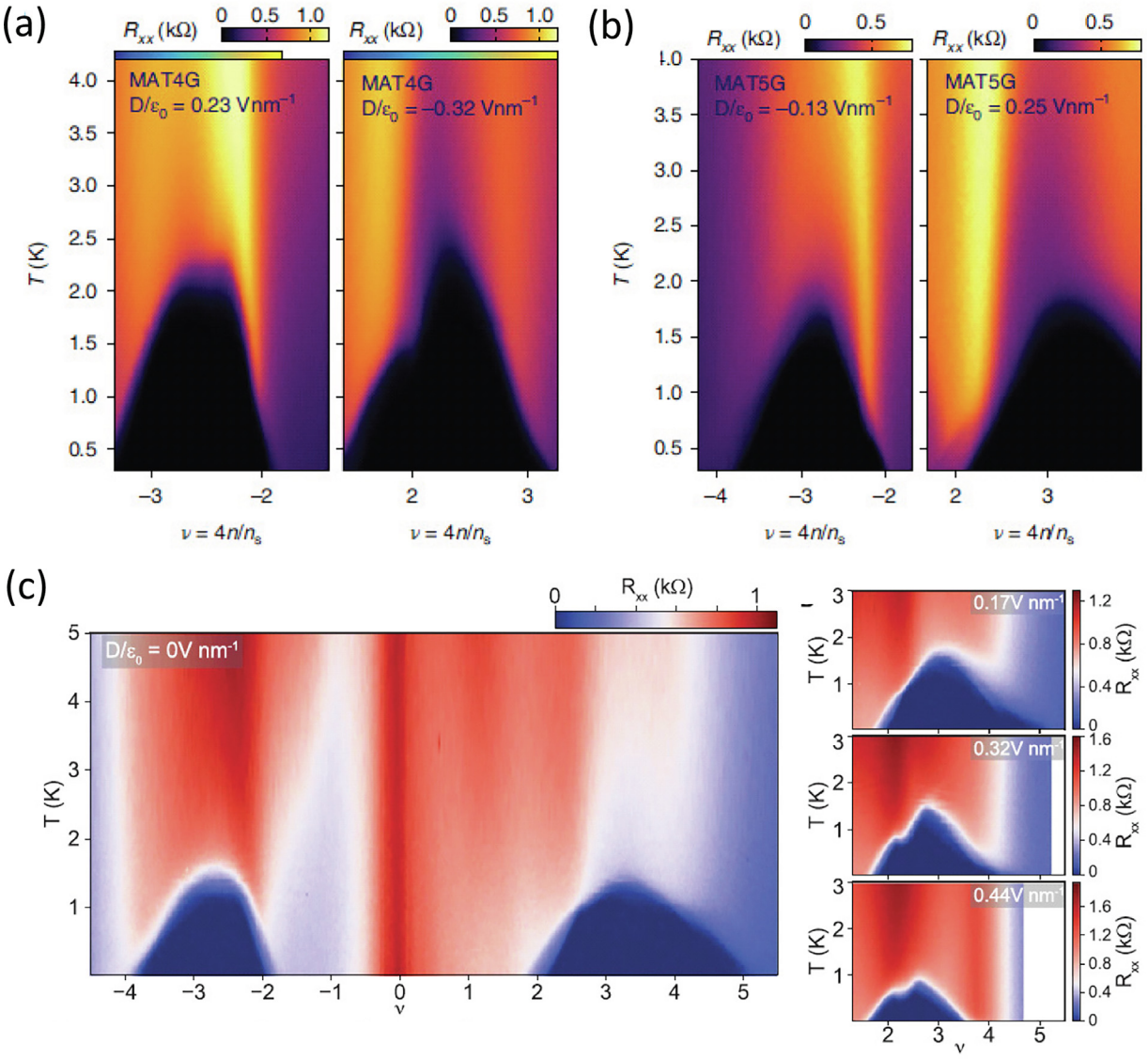

Fig. 7. (a,b) Resistance R_{xx} versus Moiré filling factor ν and temperature T for MAT4G and MAT5G. The superconducting domes span a wide density range across the flat bands, indicating robust superconductivity in these devices. One should note also that in MATTG, MAT4G and MAT5G, ν includes the filling of both the flat bands and the extra dispersive bands. Reproduced with permission from Ref. [16]. (c) R_{xx} versus n and temperature at zero D field for twisted pentalayer graphene. (d) R_{xx} versus temperature and n on the electron side at a displacement field $D = D/\varepsilon_0 = 0.17$, 0.32, and 0.44 V nm^{-1}. Reproduced with permission from Ref. [17].

In Fig. 9, the available literature data of MATBG for $T_{c,\mathrm{opt}}$ are plotted versus the Moiré angle, Θ. One can see that the highest $T_{c,\mathrm{opt}}$ is obtained at the magic angle of 1.1°, but the area of superconductivity spans the entire region from ~0.8° to ~ 1.6°, where $T_{c,\mathrm{opt}}$ is found to be at higher values for $\Theta > 1.1°$ as compared to $\Theta < 1.1°$. The application of high pressure (1.33 GPa) to the MATBG device as well as the increased size of the h-BN layer was found to lead to higher values of $T_{c,\mathrm{opt}}$, which represents an important experimental finding.

Fig. 10 presents another important development, i.e., the first STM/STS measurements on MATBG [47] and MATTG [13] devices. Although also these tunneling experiments suffer from the quite high resistance, the experiments can resolve the superconducting gaps and enable interesting information on the nature of superconductivity to be obtained. Oh et al. [47] have shown that the tunnelling spectra below the transition temperature T_c are inconsistent with those of a conventional s-wave superconductor, but rather resemble those of a nodal superconductor with an anisotropic pairing mechanism. A large discrepancy between the tunnelling gap ΔT, which far exceeds the mean-field BCS ratio (with $2\Delta T/k_B T_c \sim 25$), and the gap δ_{AR} extracted from Andreev reflection spectroscopy ($2\Delta_{\mathrm{AR}}/k_B T_c \sim 6$) was found. Furthermore, the tunnelling gap persists even when the superconductivity is suppressed, which indicates its emergence from a pseudogap phase. Moreover, the pseudogap and superconductivity are both absent when MATBG is aligned with hexagonal boron nitride. Adjacent to the coherence peaks, pronounced dip–hump features in the tunnelling conductance were observed that persist over a broad doping range (see Fig. 10a,b and d,e). The positive and negative voltage dips are typically symmetric in energy, independent of the filling. This clearly rules out the possibility that the dip-hump structures are intrinsic to background density of states.

Similar dip-hump features were observed spectroscopically in a variety of both conventional strongly coupled phonon superconductors [112,113] as well as in unconventional cuprate, iron-based and heavy fermion superconductors [114–120]. Such features are usually interpreted as a signature of bosonic modes that mediate superconductivity and can thus provide key insight into the pairing mechanism [121,122]. If a superconductor exhibits strong electron–boson coupling, dip-hump signatures are expected to appear at energies

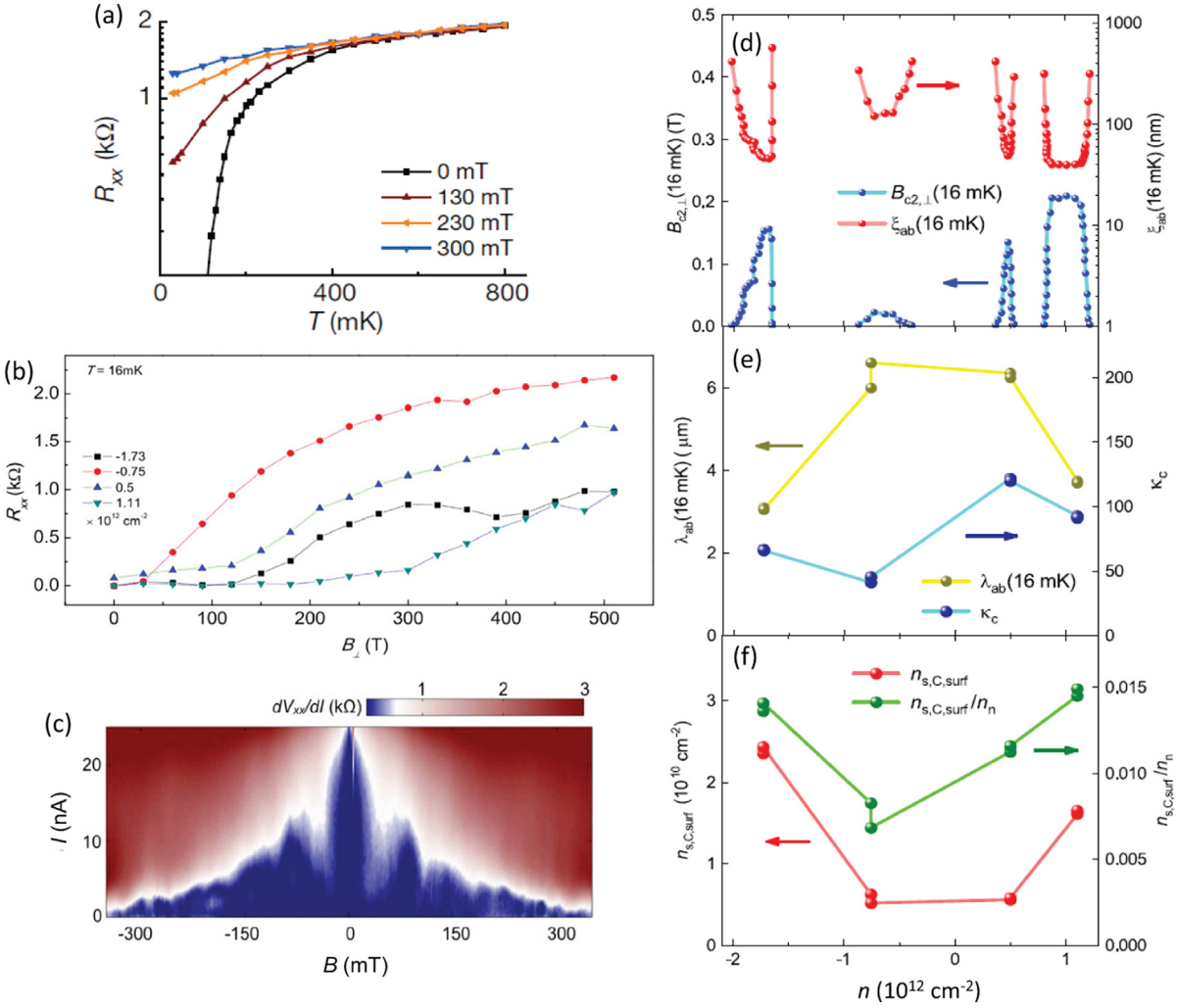

Fig. 8. The effect of applying external magnetic fields on the superconducting state of tBLG. (a) Longitudinal resistance plotted against temperature at various out-of-plane magnetic fields, showing that normal levels of resistance are restored at magnetic fields larger than 300 mT. (b) Line cuts R_{xx} vs. $B_\perp$ for each of the SC pockets taken at 16 mK at the optimal doping level. (c) Fraunhofer interference pattern measured in the superconducting state with a charge carrier density of 1.11 $\times 10^{12}$ cm^{-2}. Figures a–c: Reproduced with permission from Lu et al. [6]. (d) Analysis of the superconducting phase diagram of tBLG with Θ∼1.1°. The upper critical field, $B_{c2,\perp}$ (16 mK), and deduced ξ_{ab} (16 mK) using Eq. (1) of Ref. [11]. (e) Deduced λ_{ab} (16 mK) and κ_c for four doping states for which I_c(self-field, 16 mK) was reported by Lu et al. (f) Cooper pairs surface density, $n_{s,C,surf}$, and the ratio of $n_{s,C,surf}/n_n$ for four doping states for which I_c(self-field, 16 mK) was reported by Lu et al. [6]. Figures d–f: Reproduced with permission from Ref. [11].

$\Pi = \Delta + \Omega$, where Δ is the spectroscopic gap defined above and Ω is the bosonic-mode excitation energy [121–123].

Kim et al. [13] write: "Signatures of MATTG superconductivity presented in this work, beyond the observation of Andreev reflection, include: (1) coherence peaks that are suppressed with temperature and magnetic field, but persist well beyond the BCS limit; (2) a pseudogap-like regime; (3) dip–hump structures in the tunnelling conductance; and (4) tunnelling conductance profiles that are not adequately fit with an s-wave order parameter, but instead are compatible with a gate-tuned transition from a gapped BEC to a gapless BCS phase with a common nodal order parameter.".

Fig. 10c gives a proposed phase diagram for MATBG (Oh et al. [47]) as a function of flat-band filling factor ν and magnetic field, $B^\perp$, in the hole-doped regime. Near $-3 < \nu < -2$, an unconventional superconducting phase can be observed at low magnetic fields, which further develops into a pervasive pseudogap regime at high magnetic fields. Several quantum Hall (abbreviated: QH) and Chern insulator are also found.

All this demonstrates how important STM/STS spectroscopy measurements can be to elucidate details about the underlying mechanisms of superconductivity. Regardless of the pairing-mechanism details, the characteristic signatures in the STS spectra, together with point (4) as mentioned before, provide unambiguous evidence of the unconventional nature of MATTG superconductivity, which, of course, also applies to the other MAT*n*G systems.

Let us here summarize the results being most important for the understanding of superconductivity in the Moiré superconductors.

New results with much higher values of T_c of MATBG were presented by Saito et al. [10], who also used the h-BN as top and bottom cover, but varied the tilt angle between 1.02° and 1.20° and the thickness of the h-BN layer between 6.7 nm and 68 nm. These experiments demonstrated that device 5 with a tilt angle of Θ = 1.10–1.15° and a h-BN thickness of 45 nm showed the highest T_c ever reported for the tBLG systems.

Stepanov et al. [9] also fabricated MATBG devices with varying the h-BN thickness between 7 and 12.5 nm. Codecido et al. [7] demonstrated superconductivity in MATBG at a much smaller angle Θ = 0.93°, so superconductivity in MATBG can exist in a wide range around the magic angle, i.e., 0.93° ⩽ Θ ⩽1.27°. Lu et al. [6] have shown a complete phase diagram of their MATBG sample with four

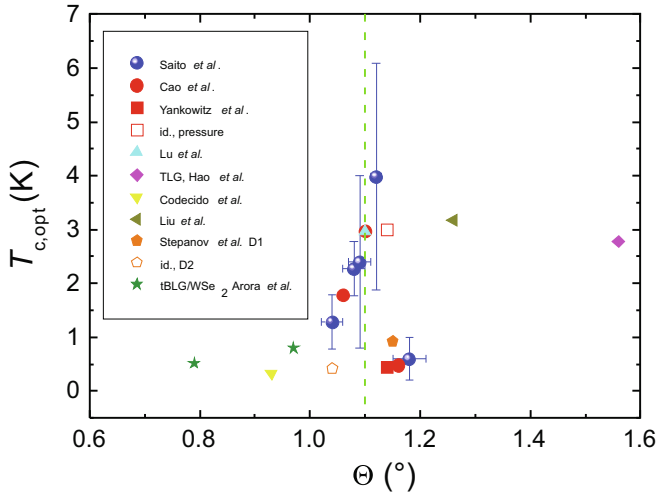

Fig. 9. Experimental data for MATBG devices of the superconducting transition temperature, $T_{c,opt}$ (defined by Saito et al. [10], which corresponds to T_c^{MF}), as function of the twist angle, Θ with the respective error bars. Data were taken from Saito et al. (Ref. [10]), together with data of Cao et al. [2], Yankowitz et al. [3], Lu et al. [6], Codecido et al. [7], Liu et al. [8], Stepanov et al. [9] and Arora et al. [18]. The dashed green line indicates the magic angle, $\Theta_{magic} = 1.1°$.

domes of superconductivity at positive and negative charge carrier densities by plotting the measured longitudinal resistance versus temperature and charge carrier density, demonstrating the experimental advances since the first reports of superconductivity in MATBG. Fig. 9 summarizes the T_c-data as function of the twist angle for various Moiré superconductors found in the literature.

The measurement of a Fraunhofer-like pattern (see Fig. 8c) solved the problem of the not observable Meissner effect in the Moiré superconductors and also demonstrated that the charge carriers in MATBG are indeed Cooper pairs. Furthermore, the analysis of the available magnetic data by Talantsev ([11], see also Figs. 8d–f) showed that the classical formulae for the self-field critical current density and the upper critical field, $H_{c2}(T)$, can be applied to the tBLG data, which implies that superconductivity of the MATBG is not so unconventional, and the extracted superconducting parameters show that only s-wave and a specific kind of p-wave symmetries are likely to be dominant.

Thus, we list here the most important findings for Moiré superconductors:

- The experiments and analyses indicated that the charge carriers in MATBG are Cooper pairs.
- The coupling mechanism is still unknown, but STM/STS spectroscopy as well as classification can provide important insights.
- The longitudinal resistance measured in the devices is in the kΩ-range, so the midpoint of the superconducting transition is recorded also in the kΩ-range. Thus, a true zero-resistance state was not yet recorded in any Moiré superconductor.
- Superconductivity in the Moiré superconductors takes place with a reduced level of superconducting charge carriers ($-n_s/2 = \sim 1.58 \times 10^{12}$ cm^{-2} for MATBG).
- The effective mass of the charge carriers is small ($m_{eff} \approx 0.2 m_e$) [1,11].
- By applying a gate voltage, doping like in a cuprate HTSc material can be simulated, and superconducting domes can appear at various values of n_s, both positive and negative, for a given Moiré angle, Θ_M (see Fig. 3). This situation corresponds directly to a 'phase diagram' seen in the cuprate HTSc materials and represents the key advantage of the MATBG devices. However, the Fermi temperature, T_F, is completely different from the HTSc as seen in the Uemura plot (see Refs. [2,11] and Fig. 11).
- The recorded Fraunhofer interference pattern ($I(B)$, [6]) manifests the superconducting character of the MATBG samples like in a Josephson contact.
- The maximum value of T_c is obtained close to the magic angle, $\Theta_{magic} = 1.1°$ (see Fig. 8). Fig. 6 also shows that T_c for $\Theta > \Theta_{magic}$ was found to be higher as for $\Theta < \Theta_{magic}$.
- Increasing the thickness of the h-BN layer as done in the experiments of Saito et al. [10] increases the maximum recorded values of T_c, but does not change the superconducting electron density ($\nu = -2.5$).

Here it is important to note that the pairing mechanism leading to the formation of Cooper pairs in Moiré superconductors remains still unknown.

Now, we can make a comparison of the Moiré superconductors to the HTSc materials, and here especially, the cuprate HTSc. For all the cuprate HTSc, the main element are the Cu–O-planes, which serve as the highway for superconductivity, and the other layers of the crystal structure serve as charge carrier reservoirs or just as spacing layers. Doping can be achieved by means of oxygenation, but also by doping with other atoms, either within the Cu–O-plane or in the charge carrier reservoir layers [124]. The main points are summarized in Table 1.

On the base of all these results collected from the literature, we may now apply the Roeser-Huber formalism to calculate the superconducting transition temperatures of the various Moiré superconductors.

4. Roeser-Huber formalism

The basic idea behind the Roeser-Huber formalism is the view of the resistive transition to the superconducting state as a resonance effect between the superconducting charge carrier wave (i.e., the Cooper pairs), λ_{cc}, and a characteristic length, $x = \lambda_{cc}/2$, in the sample. Recently, a nice discussion of the critical deBroglie wavelength in superconductors was given by Talantsev [125]. The details of the Roeser-Huber formalism were already discussed previously in Refs. [73,74,79]. To avoid possible misunderstanding, we must point out here that the Roser-Huber formalism is *not* a theory explaining the mechanism of superconductivity, nor does this approach make any use of existing theories like the BCS theory. The goal of the Roser-Huber approach is to establish a relation between superconductivity (carried by Cooper pairs) and a characteristic length in the given crystal structure, which was often demanded in the literature [92], but could not be established using the common theories.

The Roeser-Huber-equation, originally obtained for high-T_c superconductors, is written as

$$\left[(2x)^2 2M_L\right] n_0^{-2/3} \pi k_B T_c = h^2 \ , \tag{3}$$

where h is the Planck constant, k_B the Boltzmann constant, x the characteristic atomic distance, T_c the superconducting transition temperature, M_L the mass of the charge carriers, and n_0 is a correction factor describing the number of Cu–O-planes in the HTSc unit cell. For $YBa_2Cu_3O_{7-\delta}$ with one Cu–O-plane per unit cell, we have $n_0 = 1$, and the compound $Bi_2Sr_2CaCu_2O_{8+\delta}$ (Bi-2212) with 2 Cu–O-planes per unit cell has $n_0 = 2$. Thus, n for MATBG is taken to be $n = 1$ as the two graphene layers at the magic angle give together one superconducting unit. A system corresponding to $n_0 = 2$ would be then a stack of two 2D layers like h-BN–MATBG–h-BN–MATBG–h-BN, where the two MATBG layers are separated by a h-BN layer. As charge carrier mass, we assume in a first approximation $M_L = 2m_e$, corresponding to a Cooper pair.

An energy, $\Delta_{(0)}$, can be introduced via

$$\Delta_{(0)} = \pi k_B T_c \ , \tag{4}$$

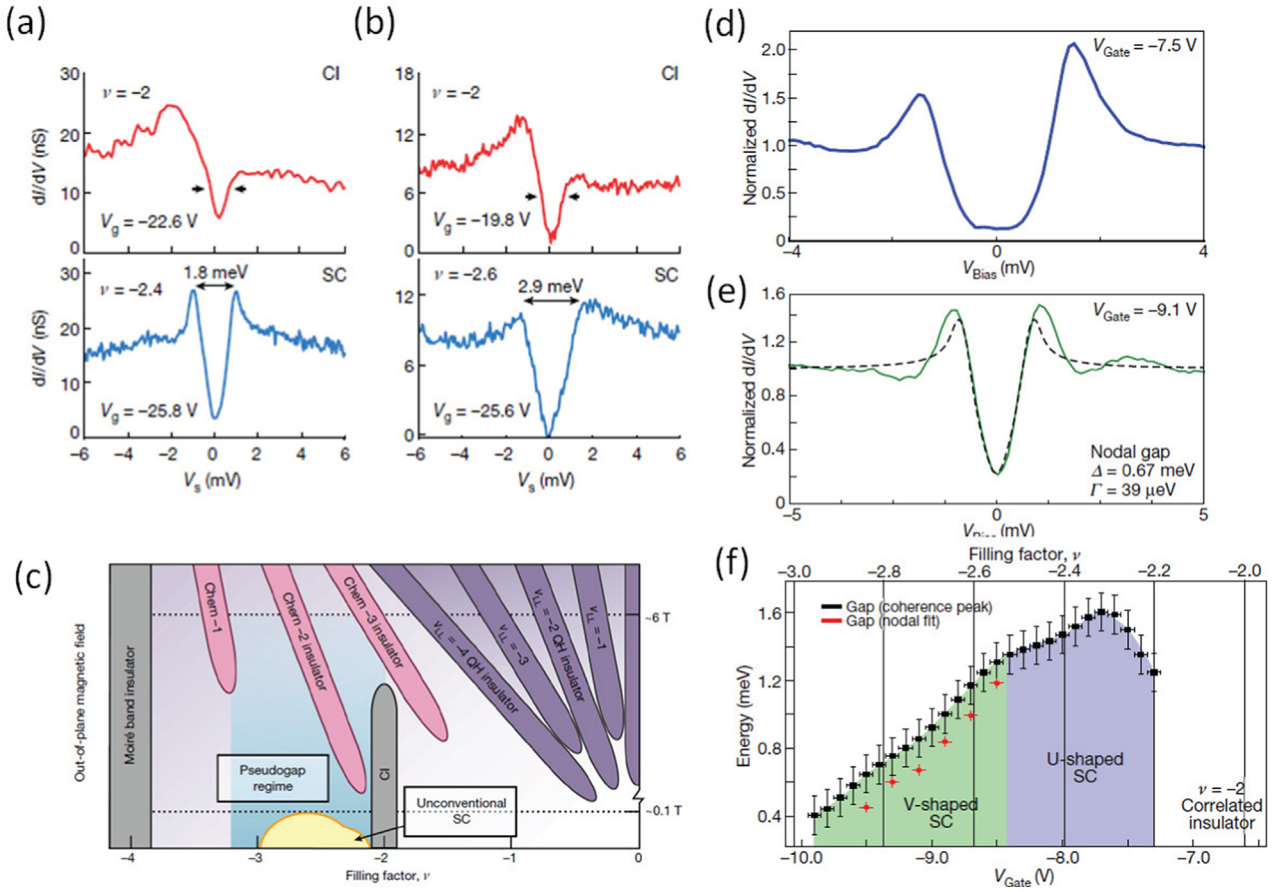

Fig. 10. STM/STS measurements on MATBG (a–c) and MATTG (d–f). (a) dI/dV(V_s) spectra for device A at $V_g = -22.6$ V (top) and $V_g = -25.8$ V (bottom). (b) dI/dV(V_s) spectra for device B at $V_g = -19.8$ V (top) and $V_g = -25.6$ V (bottom). (c) A proposed phase diagram for MATBG as a function of flat-band filling factor ν and magnetic field, $B^{\perp}$, in the hole-doped regime. (ν_{LL} is the Landau-level filling factor.) Near $-3 < \nu < -2$, an unconventional superconducting phase can be observed at low magnetic fields, which transitions into a pervasive pseudogap regime at high magnetic fields. 'QH' stands for 'quantum Hall'. Reproduced with permission from Oh et al. [47]. (d) Normalized spectra showing U-shaped and V-shaped (e) tunnelling suppression. The data are normalized by a polynomial background, and fit to the Dynes formula (e) with a nodal superconducting order parameter. (e) Gap size Δ versus ν (V_{Gate}) extracted from a half of a separation between the coherence peaks. The red markers indicate the gap size extracted from the nodal gap fit. The error bars are set by the experimental resolution (0.1 meV) and standard error of the fits. Reproduced with permission from Ref. [.13].

which may correspond to the pairing energy of the superconductor. So we can write

$$(2x)^2 \cdot 2M_L n_0^{-2/3} \cdot \Delta_{(0)} = h^2 \ . \tag{5}$$

Using Eq. (4) and regrouping of the terms leads finally to

$$\Delta_{(0)} = \frac{h^2}{2} \cdot \frac{1}{M_L} n_0^{2/3} \cdot \frac{1}{(2x)^2} = \pi k_B T_c \ . \tag{6}$$

It is important to note here that Eq. 6 was reached without the use of any theoretical description of superconductivity, just by the simple quantum mechanics model of a particle in the box [126]. Here, we must note that Eq. 3 does not offer many parameters to adapt the formalism described above to the case of MATBG and its derivatives. Thus, only minor adapations can be made: (i) taking $n_0 = 1$ was already mentioned before. (ii) M_L corresponds to the mass of a Cooper pair, so $M_L = 2m_e$. (iii) The Moiré lattice constant, a_M, plays the key role to describe the crystal parameter of a Moiré superconductor, so the characteristic length corresponds to $x = a_M$.

An essential issue to apply the Roeser-Huber formalism is the correct choice for the superconducting transition temperature, T_c. For a proper comparison of the calculated data to the experiments, T_c in the Roeser-Huber formalism is to be taken from resistance measurements as the maximum of the derivative, dR/dT, corresponding to the mean field transition temperature T_c^{MF}, which also plays an important role for the fluctuation conductivity analysis as described in Refs. [127–129]. In the literature, T_c is often derived often from 50% of the normal-state resistance, which is not necessarily the same as T_c^{MF}, especially not in the case of a two-step transition. Both these definitions of T_c are distinct from the T_c used in the Uemura plot (see Fig. 11 and Refs. [2,11,130,131]), where the completed transition when reaching $R = 0\ \Omega$ is considered. Other authors also have used $T_{(BKT)}$, the Berezinskii–Kosterlitz–Thouless (BKT) temperature, which is well suited for describing the superconducting transition in 2D systems like the ones investigated here. Most of the approaches mentioned here have, however, problems to give a proper value of T_c when the superconducting transition is very broad, shows a secondary step, does not reach $R = 0\ \Omega$ or when the deviation from the normal-state resistivity is difficult to be defined.

Thus, in the present work all the published resistance data of Moiré superconductors were digitalized and the derivative, dR/dT, was plotted graphically to obtain values for T_c according to the demands of the Roeser-Huber formalism.

5. Application of the Roeser-Huber formalism to Moiré superconductivity

The results discussed in Section 3 now provide the base to compare the results of the Roeser-Huber calculations with a wider experimental

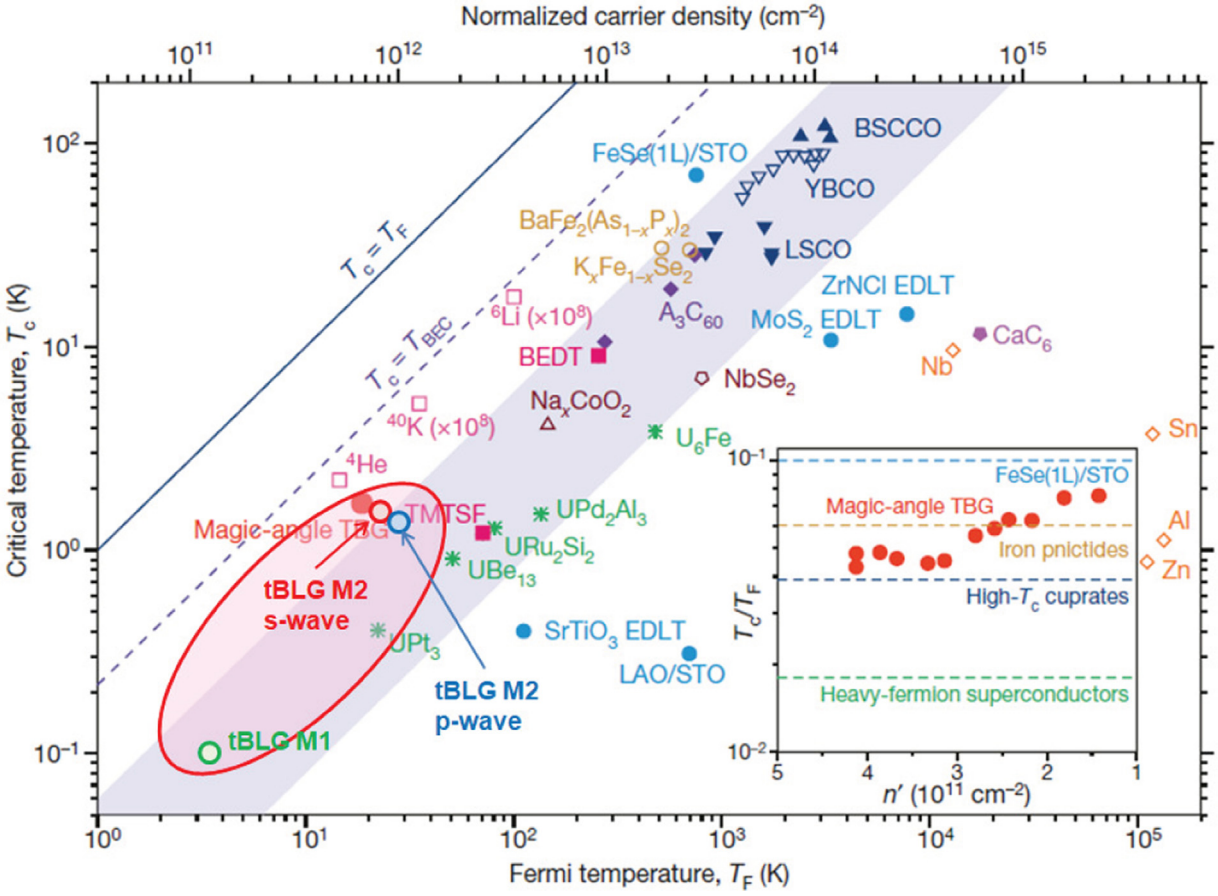

Fig. 11. Uemura plot showing the position of MATBG (●) at optimal doping ($n_{2D} = 1.5 \times 10^{11}$ cm^{-2} and $m^* = 0.2m_e$) among other most other superconducting materials. The blue shaded region is the approximate region in which almost all known unconventional superconductors are located. Abbreviations: YBCO ($YBa_2Cu_3O_{7-\delta}$, LSCO ($La_{2-x}Sr_xCuO_4$, BSCCO ($Bi_2Sr_2Ca_2Cu_3O_y$, LAO ($LaAlO_3$), STO ($SrTiO_3$), 1L (single layer), EDLT (electric double-layer transistor), BEDT (bisethylenedithiol), TMTSF (tetramethyltetraselenafulvalene). Figure reproduced with permission from Cao et al. [2]. Additional calculated data for tBLG from Talantsev et al. [11] were added into this graph as ○, MATBG M1, ○, MATBG M2 s-wave, ○, MATBG M2 p-wave and the region for MATBG is marked by a red ellipse. The inset shows T_c/T_F as function of the doping, $n\prime$. The dashed lines give the approximate T_c/T_F for heavy-fermion superconductors (▪▪▪▪), the HTSc cuprates (▪▪▪▪), the iron pnictides (▪▪▪▪) and the monolayer (1L)-FeSe on $SrTiO_3$ (STO) (▪▪▪▪). Data for MATBG are given by the red dots (●) [2].

Table 1
Table showing the differences between HTSc and Moiré superconductors.

	Moiré superconductors	cuprate HTSc
layered material	min. 2 twisted layers graphene, magic angle Θ_M twisted WSe_2 layers	Cu–O-planes
superconducting electron density, n_s	1.58×10^{12} cm^{-2}	~1×10^{14} cm^{-2}
superconducting charge carriers	Cooper pairs	Cooper pairs
charge carrier mass	0.2 m_e	
Fermi temperature	~ 10 K	~1100 K
tunability of T_c	yes, via gate voltage	yes, via oxygenation or ion doping
Meissner effect	not observable (Fraunhofer pattern)	yes (magnetic measurements)

dataset. For the Moiré superconductors, the characteristic length of the crystal structure required by the Roeser-Huber formalism is the Moiré lattice constant, a_M. However, from the data presented in Section 3, it is obvious that the various superconducting pockets or domes recorded in the phase diagrams (see Fig. 3) depend on the charge carrier concentration, n_s, for a given a_M, so $T_c(a_M, n_s)$.

For the comparison, we employed the data of Saito et al. (their Fig. 3)c, and those of Refs. [2,3,6,8,7,9,18]. The $T_{c,opt}$ determined by Saito et al. corresponds directly to T_c^{MF} required by us, so the data can be directly compared to each other as done in Table 2 below.

Table 2 presents the T_c-values of several tBLG devices of various authors [2,3,6,8,7,9,10] together with data of a graphene tri-layer [12], the data of WSe_2-stabilized tBLG [18] and the data obtained on twisted WSe_2 bi-layers [19]. Listed are the tilt angle Θ, the experimentally determined value of $T_c(\text{exp})$ corresponding to our definition of T_c^{MF}, the characteristic length, x, corresponding to the Moiré lattice constant a_M, the energy $\Delta_{(0)}$ calculated using $n_0 = 1$, $M_L = 2m_e$ and the calculated values of $T_c(\text{calc})$.

The first two rows of Table 2 give the data for tBLG at exactly the magic angle, $\Theta = 1.1°$, yielding 4.23 K with $n_0 = 1$. Using $n_0 = 2$

Table 2
Table giving the experimental data of T_c, the angles and the resulting characteristic length, $x = a_M$, the calculated energy $\Delta_{(0)}$ and T_c(calc) using the Roeser-Huber equation (Eq. 3 with $n = 1$ and $M_L = 2m_e$. The energy $\Delta^*_{(0)}$ and the transition temperature T^*_c(calc) are calculated using the correction factor η. Furthermore, the sample names of the original publication and the references are given. The T_c marked by †is the value claimed by the authors from a two-step transition. Our T_c determined from their data is $T_c = 0.32$ K. ‡This value gives the zero resistance. Stars (*) mark the WSe_2 T_c-data from the experiments of An et al. [19], where the T_c values given are determined by us. ($^{\otimes}$) as given by the authors for $R = 0$ Ω. (**) indicates T_c determined via a 50% normal-state resistance criterion.

type	tilt angle Θ [°]	T_c(exp) [K]	$x = a_M$ [nm]	$\Delta_{(0)}$ [10^{-22} J]	T_c(calc) [K]	$\Delta^*_{(0)}$ [10^{-22} J]	T^*_c(calc) [K]	η	comment	Reference(s)
MATBG	1.1	–	12.81	1.84	4.23	—	—	—	$n_0 = 1$	magic angle
	1.1	–	12.81	2.91	6.71	—	—	—	$n_0 = 2$	
MATTG	1.53	–	9.21	3.55	8.18	—	—	—	$n_0 = 1$	
MAT4G	1.75	–	8.05	4.64	10.7	—	—	—	$n_0 = 1$	
MAT5G	1.87	–	7.54	5.3	12.2	—	—	—	$n_0 = 1$	
MAT∞G	2.2	–	6.41	7.33	16.9	—	—	—	$n_0 = 1$	
MATBG	1.16	0.5	12.15	2.04	4.70	0.20	0.47	20	M1	Cao et al. [1,2]
(exp)	1.05	1.7	13.42	1.67	3.85	0.74	1.70	4.52	M2	Cao et al. [1,2]
	1.14	0.6	12.36	1.97	4.54	0.20	0.45	20	D1	Yankowitz et al. [3]
	1.27	3	11.10	2.45	5.64	1.30	3.01	3.75	D2	Yankowitz et al. [3]
									(1.33 GPa)	
	1.08	2.3	13.05	1.77	4.88	0.98	2.27	3.6	device 1	Saito et al. [10]
	1.09	2.4	12.93	1.80	4.15	1.04	2.41	3.45	device 2	Saito et al. [10]
	1.04	1.3	13.55	1.64	3.78	0.56	1.3	5.84	device 3	Saito et al. [10]
	1.12	4	12.58	1.90	4.39	2.61	3.99	2.2	device 5	Saito et al. [10]
	1.18	0.6	11.94	2.11	4.87	1.79	0.60	16.2	device 4	Saito et al.[10]
	1.1	2.3	12.81	1.84	4.23	1.29	0.96	3.8	max. T_c	Lu et al. [6]
	0.93	<0.5 †	15.16	1.31	3.02	0.14	0.32	18.9	smallest Θ	Codecido et al. [7]
	1.26	<3.5 ‡	11.19	2.41	5.55	1.38	3.17	3.5	–	Liu et al. [8]
	1.15	0.9	12.26	2.01	4.63	0.40	0.93	10	D1	Stepanov et al. [9]
	1.04	0.4	13.55	1.64	3.78	0.79	0.4	19	D2	Stepanov et al. [9]
MATTG	1.56	2.7	9.04	3.69	8.51	1.19	2.78	6.2	alternate ±Θ	Hao et al. [12]
	1.52	2.5	9.27	3.5	8.1	1.08	2.49	6.5		Zhang et al. [17]
MATBG +	0.97	0.8	14.53	1.43	3.29	0.35	0.80	8.2	D1	Arora et al. [18]
WSe_2	0.79	0.5	12.73	0.95	2.18	0.23	0.52	8.4	D3	
bi-layer	1	3.3*	18.89	0.844	1.95 ($n_0 = 1$)	—	—	—	E7,-14.4 V	An et al. [19]
WSe_2	1	$3^{\otimes}$	18.89	1.340	3.09 ($n_0 = 2$)	—	—	—	–,–	
	1	$3^{\otimes}$	20	0.753	1.74 ($n_0 = 1$)	—	—	—	–,–	
	1	$3^{\otimes}$	20	1.195	2.76 ($n_0 = 2$)	—	—	—	–,–	
	2	4.5*	9.45	3.376	7.78 ($n_0 = 1$)	1.963	4.53	3.44	F2,-6.65 V	
	2	6.1*	9.45	3.376	7.78 ($n_0 = 1$)	2.648	6.11	2.55	F2,-6.92 V	
	4	6 (50%)**	4.72	13.5	31.1 ($n_0 = 1$)	—	—	—	D11,-17.9 V	
MAT4G	1.77	2	7.96	4.75	10.9	0.86	2	10.9	alternate ±Θ	Park et al. [16]
	1.8	1.3	7.83	4.91	11.3	0.86	1.3	17		Zhang et al. [17]
MAT5G	1.84	2.2	7.66	5.13	11.8	0.95	2.2	10.8	alternate ±Θ	Park et al. [16]
	1.82	1.5	7.74	5.02	11.6	0.67	1.5	15		Zhang et al. [17]

would lead to a T_c of 6.714 K, which is even higher and unrealistic. So the choice $n_0 = 1$ is fully justified for tBLG. Table 2 shows further that the experimental variation of the tilt angle between 0.93° (the smallest tilt angle reported for superconductivity in MATBG) and 1.18° leads to T_c(calc)-values of pure tBLG ranging between 3.024 K and 4.867 K. For MATTG, MAT4G and MAT5G (rows 4–6) with their alternate twisting with ±Θ at the calculated magic angles, it is obvious that the smaller a_M leads to uch higher values of T_c as recorded experimentally. Thus, the calculated values for T_c(calc) turn out to be much larger as the experimentally observed values for T_c given in Table 2 below. What could be the reason for this?.

There are two possible scenarios to explain this outcome.

(1) The effective Moiré lattice parameter in the final devices is much larger as determined by Eq. (1).

This situation is possible when considering the fact that Moiré superlattices can be formed by all layers involved forming the device, not only the graphene bilayer as intended. This was also mentioned as possible source for errors by Saito et al. [10] when varying the h-BN thickness. The fully encapsulated graphene has necessarily two interfaces with the h-BN layers on the top and bottom, where an extra tilt can occur. Looking at Fig. 1c and Eq. (1), the effect is largest at very small angles.Thus, attempting to align the top and bottom h-BN layer to the graphene may generate much larger Moiré superlattice (MSL) parameters. Such a situation was discussed by Wang et al. [56].

In case of a stack of h-BN with graphene, there is a misfit between the two lattices, so the resulting superlattice can be described as [3,58]

$$a_{\mathrm{MSL}} = \frac{(1+\delta)a_0}{\sqrt{2(1+\delta)(1-\cos\Phi)+\delta^2}} \quad , \tag{7}$$

where δ denotes the lattice mismatch between h-BN and graphene (1.8 %) and Φ is the twist angle of h-BN with respect to graphene. A result of this is that the largest possible Moiré lattice constant is ~ 14 nm, which occurs when the one graphene layer is fully aligned to the h-BN layer. Wang et al. showed that they can increase the MSL lattice parameter to 29.6 nm by aligning both h-BN layers to the graphene. Calculating T_c with this MSL parameter would yield a value of ~0.8 K, which would be much closer to the experimental data.

However, the high pressure experiment of Yankowitz et al. [3] and the data of Saito et al. [10] demonstrated that this explanation cannot be the solution of the present problem. The optical images of the devices presented by Cao et al. [2], Yankowitz et al. [3] and Saito et al. [10] showed all arrangements made before putting the top h-BN layer in place. Thus, the misfit would be created when placing this layer. While this scenario might have applied to the first reports of superconducting tBLG, all authors of the more recent contributions have explicitly checked for such effects and even provided a dedicated discussion in their Supplementary Data (see, e.g., Fig. S2 of Ref. [6]), so this effect can be ruled out as the main reason. Furthermore, the high-pressure experiment could increase T_c from 0.6 K to 3 K with the same configuration, and the data of Saito et al. [10] showed that their experimental values of T_c are approaching the data for T_c(calc) using $M_L = 2m_e$.

(2) The choice of $M_L = 2m_e$ does not properly describe the Moiré superconductors. As seen from the Uemura plot of Fig. 7, the Fermi temperature, T_F, which includes both the effective mass of the charge carriers as well as the charge carrier density, is located for MATBG in a completely different position as the cuprate HTSc or metallic superconductors.

Eq. 3 in its present shape does not contain a parameter accounting for the small charge carrier density in the Moiré superconductors, nor is there a possibility to choose the right charge carrier density for a specific superconducting dome.

In the original derivation of the RH-formalism, it was necessary to consider the number of Cu–O-planes of the HTSc cuprates explicitly to obtain proper values for T_c(calc). This was achieved by a comparison with the Fermi energy, E_F, for a system of non-interacting fermions. E_F is the kinetic energy of the fastest fermion moving with the Fermi velocity, v_F. With the Pauli exclusion principle E_F for N particles in a box is given by [126]

$$E_F = E_{N/2} = \frac{h^2}{8m_e x^2}\left(\frac{N}{2}\right)^2. \tag{8}$$

Considering the charge carrier density, N_c, which is important for the practical case, the energy is connected to the carrier density via $E_F \sim (N_c)^{2/3}$ [73,74]. Comparing now the lowest level energy of the PiB approach, $E_1 = \frac{h^2}{8M_L x^2}$ with the Fermi energy, $E_F = \frac{h^2}{8M_{\mathrm{eff}}} N_c^{2/3} \left[\frac{3}{\pi}\right]^{2/3}$ enables a practical expression to be found: If the charge carrier density, N_c, increases by a factor n, the Fermi energy increases by $E_F \sim (nN_c)^{2/3} = n^{2/3}(N_c)^{2/3}$ [76]. So, the parameter n_0 was then defined as an integer number describing the number of the Cu–O planes and included into the formalism. Having a material with two Cu–O planes, the number of charge carriers doubles, so higher T_c(calc) values can be reached.

This observation implies that a similar approach could be made here to account for the much lower charge carrier density in the case of the Moiré superconductors. However, the Fermi energy, E_F, contains both the effective mass, M_{eff}, and the charge carrier density, N_c. Thus, the different character of M_{eff} as compared to the HTSc must be considered as well in the Roeser-Huber formalism. Band structure calculations and quantum oscillation measurements [2] revealed a small mass of the charge carriers in MATBG [2], so this change of the charge carrier mass could be implemented in the mass, M_L as used in the Roeser-Huber formalism.

A very important point is further that the Roeser-Huber formalism allows another test of the calculated data, the so-called Roeser-Huber plot [73,74,79]. It was found that all the superconducting materials investigated up to now (HTSc, metallic superconductors) fall on a common correlation line with a slope $h^2/(2\pi k_B) = 5.061 \times 10^{-45}$ m^2 kg K. This line is drawn as dashed red line (▪▪▪▪▪) in Fig. 12. The black squares (■) correspond to the data obtained for various metals and HTSc as published in Ref. [79]. The linear fit to these data (dashed-blue line, ▪▪▪▪▪) is almost perfect (i.e., close to the dashed red line) with only a small error margin, which manifests the basic idea of the Roeser-Huber formalism.

Now, we plot the calculated T_c(calc) values for the MATBG samples in the same graph using half-filled symbols. The basic data for various Moiré lattic parameters, a_M = 0.7°, 1.1° and 1.3°, are shown by the violet circles. The light green up-triangles give T_c(calc) for the devices D1, D2 (Yankowitz) and device 5 (Saito). We see that all these values lie on a nearly straight line which is located on the left side of the correlation line indicating a clear misfit of the parameters entering the calculation. The Roeser-Huber plot contains the mass, M_L on its y-axis and T_c on the x-axis. Thus, T_c and M_L for each material is a correlated data pair. When plotting the data determined for the y-axis versus the experimentally determined T_c's, we obtain the dark green left triangles, which is now crossing the correlation line. This now indicates that especially the parameter M_L is wrongly determined.

Thus, the introduction of a new factor to the RH equation is fully justified. Furthermore, it was shown by Lu et al. [6] that several superconducting domes can be found when plotting the linear resistance, R_{xx}, versus charge carrier density and temperature (see Fig. 4), which equals a phase diagram of MATBG. Thus, this fact must be accounted for in the Roeser-Huber formalism. These data of the complete phase

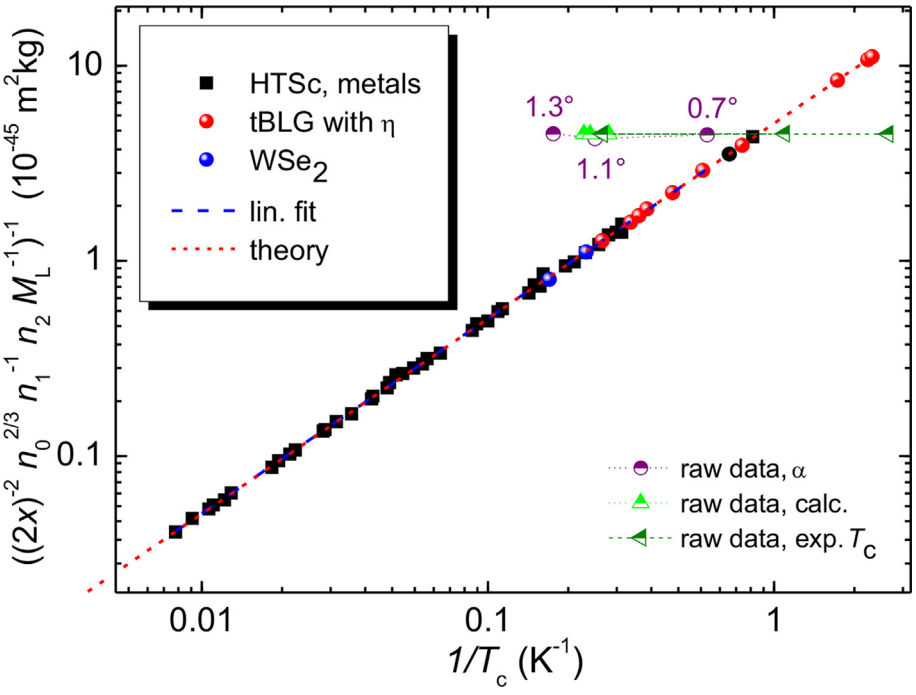

Fig. 12. Roeser-Huber plot including the data of the various MATnG samples (●) and WSe_2 (●) and the previously calculated data for several HTSc and metals/alloys (■). The straight red-dotted line follows the equation for a particle in a box [126] and the blue dashed line gives the linear fit to the data (see text).

Table 3
Table showing the data for the superconducting (sc) domes found by Lu et al. [6] for various n in a tBLG device with $\Theta = 1.1°$. T_c(exp) are data by Lu et al. T_c^{MF} was determined from the derivatives of the data shown in Fig. 2b.

sc dome	T_c(exp) (K)	T_c^{MF} (K)	n (10^{12} cm^{-2})	$\Delta^*_{(0)}$ (10^{-22} J)	T_c^*(calc) (K)	η
(1)	3	2.23	−1.73	0.96	2.23	3.8
(2)	0.65	0.59	1.11	0.25	0.58	14.5
(3)	0.16	0.16	−0.75	0.07	0.15	55
(4)	0.14	0.15	0.5	0.07	0.15	55

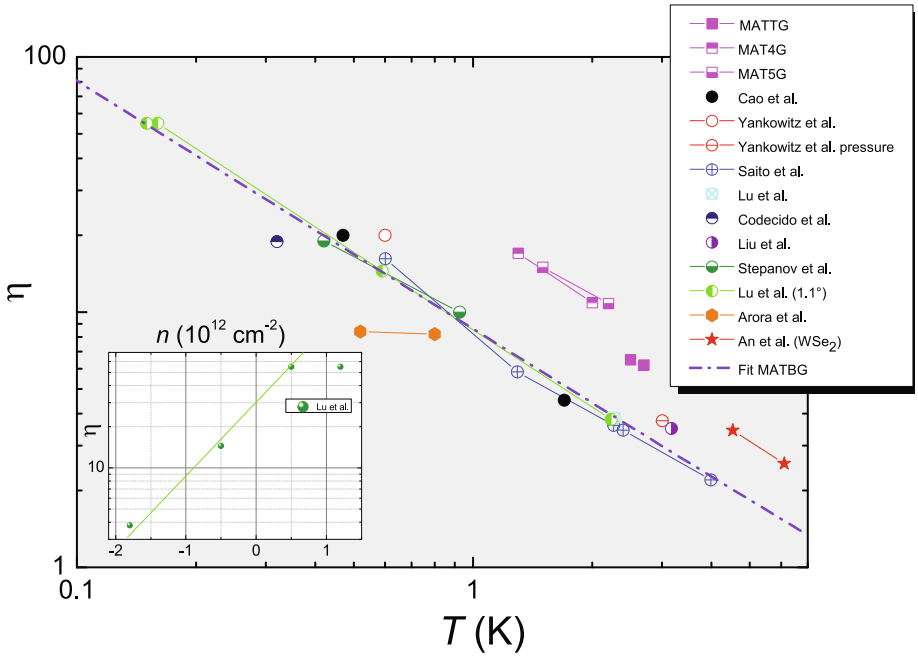

Fig. 13. The factor η as function of temperature. Included here are the MATBG data of Refs. [2,3,6,8,7,9,10], the trilayer graphene (MATTG) of Hao et al. and Zhang et al. (□, [12,17]), the MATBG/WSe_2 of Arora et al. (■, [18]) and the 2° WSe_2 data of An et al. (⊞, [19]). MAT4G and MAT5G [16,17] are shown using half-filled, violet boxes. The violet line (—) represents a fit to all MATBG data. It is obvious that the slopes for MATTG, MAT4G, MAT5G and even WSe_2 are similar to MATBG, whereas the data of Arora et al. follow a different trend. The inset shows η as function of the charge carrier density, n, using the data of Lu et al. [6] (see Table 3) with the same twist angle. A possible linear fit yields a slope close to 1/3 which corresponds to Eq. 10.

diagram furthermore offer a possibility to determine η for a sample with fixed angle Θ. In Fig. 2b, the resistance curves were presented for this sample as well [6], so one can determine the required T_c^{MF} data directly.

Table 3 gives the data of the four superconducting domes of Lu et al. [6]. T_c(exp) are the data determined by Lu et al., and the data determined by the Roeser-Huber formalism with $M_L = \eta m_e$. The values for η range between 3.8 and 55.

Cao et al. [2] and Talantsev [11] showed that in MATBG the effective mass of the charge carriers is only 0.2 m_e, and in the Uemura plot [130,131] (their Fig. 6 and our Fig. 11), they demonstrated that the MATBG samples are located at *low* Fermi temperatures $T_F \approx$ 20 K and $n_{2D} = 1.5 \times 10^{11}$ cm^{-2}, being clearly distinct from the cuprate HTSc ($T_F \approx$ 1100, see also Table 1), where the choice $M_L = 2m_e$ applies very well. Here, we can note that T_F(cuprate HTSc)/T_F(MATBG) yields ~55, and the highest T_F for MATBG is ~100, i.e., T_F(cuprate HTSc)/T_F(MATBG) ≈ 11.

Now, it is the question how this new factor η should look alike. The main problem is now that both m^* and n enter the equation for the Fermi energy. To get an idea of the required values, we may use the experimentally available data for T_c and plot these data versus the required factor, η. We determine the values for η by an iteration procedure allowing only two decimal digits. The result of this procedure is shown in Fig. 13 as a double-log graph of η as function of T. The dashed green line indicates the bottom value of $\eta = 2$, which corresponds to the case of HTSc materials. The lower the measured transition temperature, the larger the parameter η. It is notable that the slope of possible linear fits are the same for all Moiré superconductors, and only the prefactors of the power law are different, which reflect the different values of n of MATTG, MAT4G and MAT5G. Also the WSe_2-data of An et al. (⊞, [19]) follow the same trend. In contrast to this, the data of Arora et al. (■, [18]) exhibit a completely different behavior.

All values obtained for η are only in a small range between 2 and 20, which is equal to the narrow window for the MATBG samples in the Uemura plot (T_c as a function of the Fermi temperature, $T_F = E_F/k_B$ with E_F denoting the Fermi energy) in a line below the various HTSc samples (see Fig. 11 and Refs. [2,11]. As T_F is directly linked to the Fermi velocity, v_F, via

$$T_F = \frac{m^* v_F^2}{2k_B} \tag{9}$$

and

$$v_F = \frac{h}{2\pi m_e}(2\pi^2 n)^{1/3}, \tag{10}$$

there is the effective mass, m^*, and the density of the charge carriers, n, directly involved. Thus, the parameter η determined here should contain all this information, which will then also enable to judge via the value of m^* the relation $m^* < 0.1m_e$, if a material can be a superconduc-

tor or not [11]. Therefore, the parameter η is by no means an artificial approach just to obtain the right T_c-values, but η contains all the essential physics (charge carrier density, charge carrier mass) to describe a given superconducting material. So, the parameter η will further contribute to reduce the calculation error(s) in the Roeser-Huber formalism existing for some other materials like the superconducting elements Nb or Re (see their position in the Uemura plot given in Fig. 11), and also solve the long-standing problem of the choice of the proton mass for M_L for metals [79], i.e., the Fermi temperature for metals is ranging between 10^4 K and 1.2×10^5 K, which is about 10 to 100 times higher as for the HTSc materials.

The inset to Fig. 13 gives η as function of n using the data of Lu et al. [6] (Table 3) with the same twist angle. Again a linear fit is possible (however, disregarding the last point in the diagram) yielding a slope close to 1/3, which fits well to Eq. 10. However, more experimental data would be necessary for a proper evaluation.

Thus, we introduce finally a factor, named η, to the charge carrier mass M_L in Eq. (3) by writing:

$$M_L = \eta m_e. \tag{11}$$

The situation $\eta = 2$ will then correspond to our initial value of 2. Now, we come back to Table 2. The energy $\Delta^*_{(0)}$ and the corresponding $T^*_c(\mathrm{calc})$ were obtained by introducing the correction factor η to the Roeser-Huber equation, which is listed as well. The parameter η was obtained by adapting the calculation procedure manually to the experimentally obtained values of T_c. The result of this procedure is that we can now fully reproduce all the experimentally observed values for T_c. The slight deviations in $T_c(\mathrm{calc})$ account for the difficulties when extracting the T_c-values. The data for the h-BN–WSe_2–MATBG–h-BN stacks of Arora et al. [18] show that the WSe_2-layer stabilizes superconductivity at angles much smaller than the magic angle, and also smaller (0.79°) as the smallest angle reported for pure tBLG. We further note that such a monolayer of WSe_2 is not superconducting on its own; Arora et al. describe the WSe_2-layer in the their paper as insulating [18].

The trilayer graphene (MATTG by Hao et al. [12] and Zhang et al. [17]) with its alternate stacking ($\Theta = \pm\Theta$ between the graphene layers) would have a quite high T_c of 8.5 K when calculating with $M_L = 2$ due to the high average value of $\Theta = 1.56°$, yielding a small a_M. Thus, the required $\eta = 6.2$ is relatively large and also lays off the fit in Fig. 13. The same applies for the MAT4G and MAT5G stacks, where even higher values for T_c(calc) are obtained. As a consequence, the needed η are around 10–15. These larger values for η manifest the findings of Park et al. and Zhang et al. that the band filling ν is much larger in these devices. This again demonstrates the need to introduce η to the RH-formalism.

For comparison, we added also the data of Arora et al. investigating tBLG + WSe_2 [18]. These authors prepared samples with quite small angles $\Theta < \Theta_M$, with the sample D3 well below the smallest Θ reported by Codecido et al. [7]. Remarkably, the WSe_2 layer between graphene and the h-BN stabilized the superconductivity also for these small angles Θ, showing the positive effect of WSe_2. For our calculations, the high value for a_M reduces T_c(calc), but not enough to reproduce the experimentally recorded low T_c(exp) values. So, the determined value for η is found to be around 8.2 and 8.4, which is again off the fit in Fig. 13.

All the data obtained by this calculation procedure are summarized in Table 2, listing $\eta, \Delta^*_{(0)}$ and $T^*_c(\mathrm{calc})$. The calculated data now reproduce the experimental data quite well. The data for $T^*_c(\mathrm{calc})$ are often somewhat lower than the experimental data, but this reflects the uncertainity to determine T_c from the experimental data, which is often taken as the maximum value recorded. All the calculated data, $T^*_c(\mathrm{calc})$ and M_L for the various tBLG samples, fit now well to the Roeser-Huber correlation line as shown in Fig. 12 using the red bullets. Also the data for WSe_2 (see below) are given in this figure (blue bullets).

The case of bi-layer WSe_2 [19] is more complicated to be solved. The first problem in the case of WSe_2 is the value for n_0 to be taken in the calculations. If a monolayer WSe_2 is superconducting itself, n_0 must be taken as 2. If only the product from two misaligned WSe_2 layers is superconducting, we would have $n_0 = 1$ like for MATBG. A first glance on Table 2 gives the idea that $n_0 = 2$ could be correct, but as seen from the combined WSe_2–tBLG-data from Arora et al. [18], we can consider $n_0 = 1$ to be the more realistic case. Thus, we have listed both cases in Table 2 to give some predictions of T_c for the WSe_2 system. As seen from Fig. 1c, the larger lattice parameter of WSe_2 will lead to slightly larger a_M for a given angle Θ, and thus, the resulting values for T_c are higher as compared to MATBG, which is also observed experimentally [19].

The main problem is now that the experiments of Ref. [19] do not convincingly demonstrate superconductivity in this system as compared to the MATBG data, where much more detailed information is available. So it is difficult to extract properly defined values for T_c from the data presented (WSe_2 bilayers with 1°, 2° and 4° misalignment). For the 1° sample (E7), T_c could be around 3.5–4 K, for the 2° sample (F^2) ~4 K (-6.65 V) or ~6 K (-6.92 V) and for the 4° sample (D11, marked by a star in Table 1), one may get T_c somewhere between 4 K and 12 K, if at all. The calculation of the Moiré pattern parameter for the 4° sample gives $a_M = 4.72$ nm, which would yield a T_c of 49.9 K (with $n_0 = 2$) or 31.13 K with $n_0 = 1$. These values for $\Delta_{(0)}$ and T_c are considerably too high and unrealistic.

As the authors show in their paper higher order Laue reflexes from electron diffraction patterns for the 1° sample, which would indicate a lattice constant of the order of 20–25 nm (instead of the calculated 18.9° using Eq. (1)), we have used 20 nm for x in Table 2 for the 1° sample and left the 4° sample out of further consideration. If we calculate T_c using $n_0 = 2$, the calculated values come quite close to the experimental data assuming T_c~ 3 K. In all cases, the superconductivity is best documented for sample F^2 (their Figs. 5a and S11), yielding a T_c of 4.53 K (-6.65 V) and 6.1 (-6.92 V) at two different gate voltages. These T_c-values are clearly higher than those of tBLG, but also smaller than the calculated value of 7.78 K ($n_0 = 1$). Determining η for this sample yields $\eta = 3.44$ and 2.55 at the two gate voltages, which are only small correction values.

In all cases, it is a pitty that experiments with a quality similar to the MAT*n*G measurements were not yet carried out by other groups.

To summarize this part, the published data of WSe_2 are not suitable for a good comparison, but when extracting T_c via the first derivative from the published data (best for sample F^2), we only require small correction factors to reproduce the experimental T_c. This would indicate that the WSe_2 bilayers have properties being more similar to that of cuprate HTSc compounds.

Coming now back to the Roeser-Huber plot of Fig. 12, the red data points (●) give the final results with the factor η for the various tBLG samples investigated in the literature (Table 2), and the blue bullet (●) shows the data of the 2° WSe_2 sample.

A more dedicated analysis of all the data available (MATBG samples as well as the extreme elemental superconductors like Bi or Li) will allow to further clarify the properties of η. Here, we can state that η is directly proportial to the effective charge carrier mass, m^*, and the charge carrier density enters the formula like the parameter n_0. For this, we may define a relation $n_d = n_s(\mathrm{MATBG})/n_s(\mathrm{HTSc})$. In this way, the different value of n_s appears as a percentage of the HTSc value, like $n_d = 0.00158$, and in the final formula as $n_d^{2/3} = 0.0136$.

Harshman and Fiory [132] presented another way of calculating the transition temperature of MATBG from experimental data. Also this approach was originally developed for HTSc samples, and the parameters involved are quite similar to those of the Roeser-Huber approach. However, there is no relation between the T_c and the crystal lattice parameters, except a distance between the superconducting layers, which in turn is not contained in the Roeser-Huber formalism. In

all cases, it will be interesting to compare the various parameters of the models with each other.

So, we can say here that an extension of the Roeser-Huber formalism is required to account for the low charge carrier densities of the Moiré superconductors and the resulting low charge carrier mass using the new parameter η. When doing so, we can directly reproduce the experimental data of the various measurements on Moiré superconductors published in the literature, and the resulting data fit very well to the correlation line of the Roeser-Huber plot (see Fig. 12). However, it is clear that such calculations are only possible when data of either bandstructure calculations or experiments are already available, so this approach cannot used for predictions of still unknown materials.

Very important is the following point: We must note here that the calculations performed using $\eta = 2$, that is, a charge carrier mass of $2m_e$, yield an upper limit for T_c of Moiré superconductors, to which the experiments come now close by applying pressure or using thicker h-BN layers (see, e.g., the results of Yankowitz [3] and Saito et al. [10]). Thus, using the Roeser-Huber formalism for Moiré superconductors *without* the specific knowledge of effective charge carrier mass and charge carrier density, provides in turn an upper limit for T_c. This observation is a very *positive* output for use of the Roeser-Huber equation to predict superconducting transition temperatures of still unknown materials (without the knowledge of n_s or m^*), but knowing the important crystal parameters and having a basic idea of the value of the Fermi temperature.

6. Conclusions and outlook

As outlook for future research in the field of Moiré superconductivity, one can state that the Moiré superlattices have developed into excellent platforms for the study of new properties of layered 2D materials in general [133], where superconductivity is only one of several special properties. The recent creation of devices with 3, 4 or more graphene layers demonstrated stable and robust superconductivity, and the finding of the dependence of T_c on the h-BN layer thickness also clearly showed that more robust superconductivity with higher T_c's is possible in the Moiré superconductors. Thus, one may expect creation of new superconducting materials by different types of stacking the layers, e.g., the combination of graphene and WSe_2 or $NbSe_2$, combinations with other flat 2D-layers like borophene, stannene [21,22], etc., or even heuslerenes [134], which may be superconducting themselves or not. In all cases, the reviewed research is only the top of an iceberg, as countless other combinations are theoretically possible. Another interesting aspect is the finding of Moiré pattern on the surface of a topological insulator [135,136], combining two ongoing research directions. Also here, more stable and robust new superconducting states may result, which will further widen up the knowledge of such unconventional superconductors.

A large challenge for the future is the fabrication of larger MAT*n*G devices with reproducible twist angles and clean surfaces as stated in Ref. [86]. This will enable many more important experiments on superconductivity to be performed and thus, foster the entire new field of twistronics [137]. Hopefully, such improved samples will allow to solve the standing problem of recording true, zero resistivity. To reach higher values of T_c, a repetition of the work of Saito et al. [10] with reproducible Moiré angles would clarify the role of the h-BN-layer thickness and thus strongly contribute to find new types of stacks with higher T_c. Furthermore, the fabrication of new types and arrangements of 2D stacked layers with new properties and possibly, stable and robust superconductivity, will enable much deeper insights to Moiré superconductivity. For the twisted superconducting WSe_2 layers, which were already discussed in the literature, the currently available experimental data are not sufficient to extract proper values for the superconducting transition temperature, T_c, to enable a proper comparison with the calculated data, thus, these experiments should be repeated. The study of such new types of stacks may receive help from machine learning-based simulations once more experiments describing the properties of various other 2D-layers are carried out to give a proper foundation for such simulation work.

To summarize up the present paper, in the first part we have given a summary of the various measurements on superconducting MAT*n*G samples as published in the literature. For the measurements, a typical structure called device was build up consisting of the twisted graphene layers, a top and bottom h-BN layer and graphite as a substrate and cover for better handling of the structure. Via electric contacts, the longitudinal resistance, R_{xx}, could be measured as function of temperature, charge carrier density, applied magnetic field, twist angle, and h-BN layer thickness. An important result is here that the complete phase diagram (in analogy to the phase diagram of cuprate HTSc) could be measured by electrically tuning the charge carrier density, n, via the gate voltage. This enables a complete study of the superconducting properties of the various MAT*n*G samples for a given twist angle of the graphene layers. Furthermore, measuring the characteristic Fraunhofer patterns enables a direct proof of the superconducting state, which is important as the classical Meissner effect can not be magnetically measured in the present MAT*n*G devices.

All the data of the superconducting state collected by various authors now enable the calculation of T_c of Moiré superconductors based on the Moiré lattice parameter using the Roeser-Huber formalism. When doing so, we find that the Roeser-Huber formula in the standard form with $M_L = 2\ m_e$ yields an upper limit of T_c for tBLG, which is approached by the experimental observations for MATBG samples under pressure or with thicker h-BN layers.

To better describe the superconducting state(s) of the various MAT*n*G samples and to account for the distinctly different Fermi temperatures found by various authors, the introduction of a new factor η to the Roeser-Huber formalism enables to account for the small charge carrier densities and charge carrier mass, so that the experimentally obtained data can successfully be reproduced. All the calculated data fit well to the correlation line in the Roeser-Huber plot. Of course, further work is required to find a theoretical foundation for the new parameter η, but it is already obvious that the Fermi temperature, T_F, containing the charge carrier density, n_s, and the effective charge carrier mass, m^*, plays an important role here. Via T_F and the corresponding Fermi velocity, v_F, it becomes even possible to introduce a criterion to the Roeser-Huber formalism to distinguish if a given material can be a superconductor or not. This will transform the RH formalism into an useful tool for finding new superconducting materials combining data bases of crystallographic data and information on superconductivity.

Data availability

The data that support the findings of this study are available from the corresponding author upon reasonable request.

Declaration of Competing Interest

The authors declare that they have no known competing financial interests or personal relationships that could have appeared to influence the work reported in this paper.

acknowledgments

The review section of this article was worked out as part of a lecture 'Nanostructure Physics'. Part of the work was supported by DFG-ANR project under the references ANR-17-CE05-0030 and DFG-ANR Ko2323-10, respectively.

References

[1] Yuan Cao Y, Fatemi V, Demir A, Fang S, Tomarken SL, Luo JY, Sanchez-Yamagishi JD, Watanabe K, Taniguchi T, Kaxiras E, Ashoori RC, Jarillo-Herrero P. Correlated insulator behaviour at half-filling in magic-angle graphene superlattices. Nature 2018;55:80–4. https://doi.org/10.1038/nature26154.

[2] Cao Y, Fatemi V, Fang S, Watanabe K, Taniguchi T, Kaxiras E, Jarillo-Herrero P. Unconventional superconductivity in magic-angle graphene superlattices. Nature 2018;556:43–50. https://doi.org/10.1038/nature26160.

[3] Yankowitz M, Chen S, Polshyn H, Zhang Y, Watanabe K, Taniguchi T, Graf D, Young AF, Dean CR. Tuning superconductivity in twisted bilayer graphene. Science 2019;363:1059–64. https://doi.org/10.1126/science.aav1910.

[4] Suárez Morell E, Correa JD, Vargas P, Pacheco M, Barticevic Z. Flat bands in slightly twisted bilayer graphene: tight-binding calculations. Phys Rev B 2010;82:121407. https://doi.org/10.1103/PhysRevB.82.121407.

[5] Trambly de Laissardière G, Mayou D, Magaud L. Localization of Dirac electrons in rotated graphene bilayers. Nano Lett 2010;10:804–8. https://doi.org/10.1021/nl902948m.

[6] Lu X, Stepanov P, Yang W, Xie M, Ali Aamir M, Das I, Urgell C, Watanabe K, Taniguchi T, Zhang G, Bachtold A, MacDonald AH, Efetov DK. Superconductors, orbital magnets and correlated states in magic-angle bilayer graphene. Nature 2019;574:653–7. https://doi.org/10.1038/s41586-019-1695-0.

[7] Codecido E, Wang Q, Koester R, Che S, Tian H, Lv R, Tran S, Watanabe K, Taniguchi T, Zhang F, Bockrath M, Lau CN. Correlated insulating and superconducting states in twisted bilayer graphene below the magic angle. Sci Adv 2019;5:. eaaw9770. https://doi.org/10.1126/sciadv.aaw9770.

[8] Liu X, Hao Z, Khalaf E, Lee J-Y, Watanabe K, Taniguchi T, Vishwanath A, Kim P. Tunable spin-polarized correlated states in twisted double bilayer graphene. Nature 2020;583:221–5. https://doi.org/10.1038/s41586-020-2458-7.

[9] Stepanov P, Das I, Lu X, Fahimniya A, Watanabe K, Taniguchi T, Koppens FHL, Lischner J, Levitov L, Efetov FK. Untying the insulating and superconducting orders in magic-angle graphene. Nature 2020;583:375–8. https://doi.org/10.1038/s41586-020-2459-6.

[10] Saito Y, Ge J, Watanabe K, Taniguchi T, Young AF. Independent superconductors and correlated insulators in twisted bilayer graphene Nat Phys 2020;16:926–30. https://doi.org/10.1038/s41567-020-0928-3.

[11] Talantsev EF, Mataira RC, Crump WP. Classifying superconductivity in Moiré graphene superlattices. Sci Rep 2020;10:212; doi: 10.1038/s41598-019-57055-w.

[12] Hao Z, Zimmerman AM, Ledwith P, Khalaf E, Najafabadi DH, Watanabe K, Taniguchi T, Vishwanath A, Kim P. Electric field–tunable superconductivity in alternating-twist magic-angle trilayer graphene. Science 2021;371:1133–8. https://doi.org/10.1126/science.abg0399.

[13] Kim H, Choi Y, Lewandowski C, Thomson A, Zhang Y, Polski R, Watanabe K, Taniguchi T, Alicea J, Nadj-Perge S. Evidence for unconventional superconductivity in twisted trilayer graphene. Nature 2022;606:494–500. https://doi.org/10.1038/s41586-022-04715-z-.

[14] Guorui Chen C, Sharpe AL, Gallagher P, Rosen IT, Fox EJ, Jiang L, Lyu B, Li H, Watanabe K, Taniguchi T, Jung J, Shi Z, Goldhaber-Gordon D, Zhang Y, Wang F. Signatures of tunable superconductivity in a trilayer graphene moiré superlattice. Nature 2019;572:215–9. https://doi.org/10.1038/s41586-019-1393-y.

[15] Park JM, Cao Y, Watanabe K, Taniguchi T, Jarillo-Herrero P. Tunable strongly coupled superconductivity in magic-angle twisted trilayer graphene. Nature 2021;590:249–55. https://doi.org/10.1038/s41586-021-03192-0.

[16] Park JM, Cao Y, Xia L, Sun S, Watanabe K, Taniguchi T, Jarillo-Herrero P. Magic-angle multilayer graphene: a robust family of Moiré Superconductors. Nat Mater 2022;21:877–83. https://doi.org/10.1038/s41563-022-01287-1.

[17] Zhang Y, Polski R, Lewandowski C, Thomson A, Peng Y, Choi Y, et al. Promotion of superconductivity in magic-angle graphene multilayers. Science 2022;377:1538–43. https://doi.org/10.1126/science.abn8585.

[18] Arora HS, Polski R, Zhang Y, Thomson A, Choi Y, Kim H, Lin Z, Wilson IZ, Xu X, Chu J-H, Watanabe K, Taniguchi T, Alicea J, Nadj-Perge S. Superconductivity in metallic twisted bilayer graphene stabilized by WSe_2. Nature 2020;583:379–84. https://doi.org/10.1038/s41586-020-2473-8.

[19] An L, Cai X, Pei D, Huang M, Wu Z, Zhou Z, Lin J, Ying Z, Ye Z, Feng X, Gao R, Cacho C, Watson M, Chen Y, Wang N. Interaction effects and superconductivity signatures in twisted double-bilayer WSe_2. Nanoscale Horiz 2020;5:1309. https://doi.org/10.1039/d0nh00248h.

[20] Balents L, Dean CR, Efetov DK, Young AF. Superconductivity and strong correlations in moiré flat bands. Nat Phys 2020;16:725–33. https://doi.org/10.1038/s41567-020-0906-9.

[21] Liao M, Zang Y, Guan Z, Li H, Gong Y, Zhu K, Hu X-P, Zhang D, Xu Y, Wang Y-Y, He K, Ma X-C, Zhang S-C, Xue Q-K. Superconductivity in few-layer stanene. Nat Phys 2018;14:344–8. https://doi.org/10.1038/s41567-017-0031-6.

[22] Yan L, Liu P-F, Li H, Tang Y, He J, Huang X, Wang B-T, Zhou L. Theoretical dissection of superconductivity in two-dimensional honeycomb borophene oxide B_2O crystal with a high stability. npj Comput Mater 2020;6:94. https://doi.org/10.1038/s41524-020-00365-9.

[23] Bistritzer R, MacDonald AH. Moiré bands in twisted double-layer graphene. Proc Natl Acad Sci 2011;108:12233–7. https://doi.org/10.1073/pnas.1108174108.

[24] Wu F, Hwang E, Das Sarma S. Phonon-induced giant linear-in-T resistivity in magic angle twisted bilayer graphene: Ordinary strangeness and exotic superconductivity. Phys Rev B 2019;99:165112. https://doi.org/10.1103/PhysRevB.99.165112.

[25] Schrade C, Fu L. Spin-valley density wave in moiré materials. Phys Rev B 2019;100:035413. https://doi.org/10.1103/PhysRevB.100.035413.

[26] Carr S, Fang S, Po HC, Vishwanath A, Kaxiras E. Derivation of Wannier orbitals and minimal-basis tight-binding Hamiltonians for twisted bilayer graphene: first-principles approach. Phys Rev Res 2019;1:033072. doi: PhysRevResearch.1.033072.

[27] Lian B, Wang Z, Bernevig BA. Twisted bilayer graphene: a phonon-driven superconductor. Phys Rev Lett 2019;122:257002. https://doi.org/10.1103/PhysRevLett.122.257002.

[28] Shi L, Ma J, Song JCW. Gate-tunable flat bands in van der Waals patterned dielectric superlattices.. 2D Mater 2020;7:015208. https://doi.org/10.1088/2053-1583/ab59a8.

[29] Kim K, DaSilva A, Huang S, Fallahazad B, Larentis S, Taniguchi T, Watanabe K, LeRoy BJ, MacDonald AH, Tutuc E. Tunable moiré bands and strong correlations in small-twist-angle bilayer graphene. Proc Natl Acad Sci USA 2017;114:3364–9. https://doi.org/10.1073/pnas.1620140114.

[30] Wallbank JR, Kumar RK, Holwill M, Wang Z, Auton GH, Birkbeck J, Mishchenko A, Ponomarenko LA, Watanabe K, Taniguchi T, Novoselov KS, Aleiner IL, Geim AK, Fal'ko VI. Excess resistivity in graphene superlattices caused by umklapp electron–electron scattering. Nat Phys 2018;15:32–6. https://doi.org/10.1038/s41567-018-0278-6.

[31] Choi YW, Choi HJ. Strong electron-phonon coupling, electron-hole asymmetry, and nonadiabaticity in magic-angle twisted bilayer graphene. Phys Rev B 2018;98:241412. https://doi.org/10.1106/Phys. Rev. B. 241412.

[32] Goodwin ZAH, Corsetti F, Mostofi AA, Lischner J. Attractive electron-electron interactions from internal screening in magic-angle twisted bilayer graphene. Phys. Rev. B 2019;100:235424. https://doi.org/10.1103/PhysRevB.100.235424.

[33] Polshyn H, Yankowitz M, Chen S, Zhang Y, Watanabe K, Taniguchi T, Dean CR, Young AF. Large linear-in-temperature resistivity in twisted bilayer graphene. Nat Phys 2019;15:1011–6. https://doi.org/10.1038/s41567-019-0596-3.

[34] Lian B, Wang Z, Bernevig BA. Twisted bilayer graphene: A phonon-driven superconductor. Phys Rev Lett 2019;122:257002. https://doi.org/10.1106/Phys. Rev. Lett. 257002.

[35] Kerelsky A, McGilly LJ, Kennes DM, Xian L, Yankowitz M, Chen S, Watanabe K, Taniguchi T, Hone J, Dean C, et al. Maximized electron interactions at the magic angle in twisted bilayer graphene. Nature 2019;572:95–100. https://doi.org/10.1038/s41586-019-1431-9.

[36] Sharpe AL, Fox EJ, Barnard AW, Finney J, Watanabe K, Taniguchi T, Kastner MA, Goldhaber-Gordon D. Emergent ferromagnetism near three-quarters filling in twisted bilayer graphene. Science 2019;365:605–8. https://doi.org/10.1126/science.aaw3780.

[37] Chu Y, Zhu F, Wen L, Chen W, Chen Q, Ma T. Superconductivity in twisted multilayer graphene: A smoking gun in recent condensed matter physics. Chin Phys B 2020;29:117401. https://doi.org/10.1088/1674-1056/abbbea.

[38] Nimbalkar A, Kim H. Opportunities and challenges in twisted bilayer graphene: a review. Nano-Micro Lett 2020;12:126. https://doi.org/10.1007/s40820-020-00464-8.

[39] Serlin M, Tschirhart CL, Polshyn H, Zhang Y, Zhu J, Watanabe K, Taniguchi T, Balents L, Young AF. Intrinsic quantized anomalous Hall effect in a moiré heterostructure. Science 2020;2020(367):900–3. https://doi.org/10.1126/science.aay5533.

[40] Das I, Lu X, Herzog-Arbeitman J, Song Z-D, Watanabe K, Taniguchi T, Bernevig BA, Efetov DK. Symmetry-broken Chern insulators and Rashba-like Landau-level crossings in magic-angle bilayer graphene. Nat Phys 2021;17:1–5. https://doi.org/10.1038/s41567-021-01186-3.

[41] He M, Li Y, Cai J, Liu Y, Watanabe K, Taniguchi T, Xu X, Yankowitz M. Symmetry breaking in twisted double bilayer graphene. Nat Phys 2021;17:26–30. https://doi.org/10.1038/s41567-020-1030-6.

[42] He M, Zhang Y-H, Li Y, Fei Z, Watanabe K, Taniguchi T, Xu X, Yankowitz M. Competing correlated states and abundant orbital magnetism in twisted monolayer-bilayer graphene. Nat Commun 2021;12:4727. https://doi.org/10.1038/s41467-021-25044-1.

[43] Li W, Reichhardt CJO, Jankó B, Reichhardt C. Vortex dynamics, pinning, and angle-dependent motion on moiré patterns. Phys Rev B 2021;104:024504. https://doi.org/10.1106/Phys. Rev. B. 024504.

[44] Ledwith PJ, Khalaf E, Vishwanath A. Strong coupling theory of magic-angle graphene: A pedagogical introduction. Ann Phys 2021;435:168646. https://doi.org/10.1016/j.aop.2021.168646.

[45] Saito Y, Ge J, Rademaker L, Watanabe K, Taniguchi T, Abanin DA, Young AF. Hofstadter subband ferromagnetism and symmetry-broken Chern insulators in twisted bilayer graphene. Nat Phys 2021;17:478–81. https://doi.org/10.1038/s41567-020-01129-4.

[46] Cao Y, Park JM, Watanabe K, Taniguchi T, Jarillo-Herrero P. Pauli-limit violation and re-entrant superconductivity in moiré graphene. Nature 2021;595:526–31. https://doi.org/10.1038/s41586-021-03685-y.

[47] Oh M, Nuckolls KP, Wong D, Lee RL, Liu X, Watanabe K, Taniguchi T, Yazdani A. Evidence for unconventional superconductivity in twisted bilayer graphene. Nature 2021;600:240–5. https://doi.org/10.1038/s41586-021-04121-x.

[48] Hu C, Wu T, Huang X, Dong Y, Chen J, Zhang Z, Lyu B, Ma S, Watanabe K, Taniguchi T, Xie G, Li X, Liang Q, Shi Z. In-situ twistable bilayer graphene. Sci Rep 2022;12:204. https://doi.org/10.1038/s41598-021-04030-z.

[49] Romanova M, Vlček V. Stochastic many-body calculations of moiré states in twisted bilayer graphene at high pressures. npj Comput Mater 2022. https://doi.org/10.1038/s41524-022-00697-8. 8,11.

[50] Ghawri B, Mahapatra PS, Garg M, Mandal S, Bhowmik S, Jayaraman A, Soni R, Watanabe K, Taniguchi T, Krishnamurthy HR, Jain M, Banerjee S, Chandni U,

Ghosh A. Breakdown of semiclassical description of thermoelectricity in near-magic angle twisted bilayer graphene. Nat Commun 2022;13:1522. https://doi.org/10.1038/s41467-022-29198-4.
[51] Klein DR, Xia L-Q, MacNeill D, Watanabe K, Taniguchi T, Jarillo-Herrero P. Electrical switching of a moiré ferroelectric superconductor. Nat Nanotechnol 2023. https://doi.org/10.1038/s41565-022-01314-x.
[52] Klebl L, Goodwin ZAH, Mostofi AA, Kennes DM, Lischner J. Importance of long-ranged electron-electron interactions for the magnetic phase diagram of twisted bilayer graphene. Phys Rev B 2021;103:195127. https://doi.org/10.1103/Phys.Rev. B. 195127.
[53] Vahedi J, Peters R, Missaoui A, Honecker A, Trambly LG. Magnetism of magic-angle twisted bilayer graphene. SciPost Phys 2021;11:083. https://doi.org/10.21468/SciPostPhys.11.4.083.
[54] Finney J, Sharpe AL, Fox EJ, Hsueh C, Watanabe K, Taniguchi T, Kastner M, Goldhaber-Gordon D. Unusual magnetotransport in twisted bilayer graphene. PNAS 2022;119:. e2118482119. https://doi.org/10.1073/pnas.211848211.
[55] Decker R, Wang Y, Brar VW, Regan W, Tsai H-Z, Wu Q, Gannett W, Zettl A, Crommie MF. Local electronic properties of graphene on a BN substrate via scanning tunneling microscopy. Nano Lett. 2011;11:2291–5. https://doi.org/10.1021/nl2005115.
[56] Wang L, Zihlmann S, Liu M-H, Makk P, Watanabe K, Taniguchi T, Baumgartner A, Schönenberger Chr. New generation of Moiré Superlattices in Doubly Aligned hBN/Graphene/hBN Heterostructures. Nano Lett 2019;19:2371–6. https://doi.org/10.1021/acs.nanolett.8b05061.
[57] Hermann K. Periodic overlayers and moiré patterns: theoretical studies of geometric properties. J Phys: Condens Matter 2012;24:314210. https://doi.org/10.1088/0953-8984/24/31/314210.
[58] Moon P, Koshino M. Electronic properties of graphene/hexagonal-boron-nitride moiré superlattice. Phys Rev B 2014;90:155406. https://doi.org/10.1103/PhysRevB.90.155406.
[59] Andelkovic M, Milovanovic SP, Covaci L, Peeters FM. Double moiré with a twist: super-moiré in encapsulated graphene. Nano Lett 2020; 9b04058; doi: https://doi.org/10.1021/acs.nanolett.9b04058.
[60] Tang K, Qi W. Moiré-pattern-tuned electronic structures of van der Waals Heterostructures. Adv Funct Mater 2020;2020:2002672. https://doi.org/10.1002/adfm.202002672.
[61] Martin I. Moiré superconductivity. Ann Phys 2020;417:116118. https://doi.org/10.1016/j.aop.2020.168118.
[62] Sun Z, Hu YH. How magical is magic-angle graphene? Matter 2020;2:1106–14. https://doi.org/10.1016/j.matt.2020.03.010.
[63] Sharpe AL. Stacks on stacks on stacks. Nat Mater 2022;21:838–47. https://doi.org/10.1038/s41563-022-01314-1.
[64] Burg GW, Khalaf E, Wang Y, Watanabe K, Taniguchi T, Tutuc E. Emergence of correlations in alternating twist quadrilayer graphene. Nat Mater 2022;21:884–9. https://doi.org/10.1038/s41563-022-01286-2.
[65] Xie S, Faeth BD, Tang Y, Li L, Gerber E, Parzyck CT, Chowdhury D, Zhang Y-H, Jozwiak C, Bostwick A, Rotenberg E, Kim E-A, Shan J, Mak KF, Shen KM. Strong interlayer interactions in bilayer and trilayer moiré superlattices. Sci Adv 2022;8: eabk1911. https://doi.org/10.1126/sciadv.abk1911.
[66] Törmä P, Peotta S, Bernevig BA. Superconductivity, superfluidity and quantum geometry in twisted multilayer systems. Nat Phys 2022;4:528–42. https://doi.org/10.1038/s42254-022-00466-y.
[67] Stanev V, Oses C, Kusne AG, Rodriguez E, Paglione J, Curtarolo S, Takeuchi I. Machine learning modeling of superconducting critical temperature. npj Comput Mater 2018;4:29. https://doi.org/10.1038/s41524-018-0085-8.
[68] Matsumoto K, Horide T. An acceleration search method of higher T_c superconductors by a machine learning algorithm. Appl Phys Exp 2019;12:073003. https://doi.org/10.7567/1882-9786/ab2822.
[69] Zeng S, Zhao Y, Li G, Wang R, Wang X, Ni J. Atom table convolutional neural networks for an accurate prediction of compounds properties. npj Comput Mater 2019;5:84. https://doi.org/10.1038/s41524-019-0223-y.
[70] Hutcheon MJ, Shipley AM, Needs RJ. Predicting novel superconducting hydrides using machine learning approaches. Phys Rev B 2020;101:144505. https://doi.org/10.1103/PhysRevB.101.144505.
[71] Lee D, You D, Lee D, Li X, Kim S. Machine-learning-guided prediction models of critical temperature of cuprates. J Phys Chem Lett 2021;12:6211–7. https://doi.org/10.1021/acs.jpclett.1c01442.
[72] Stanev V, Choudhary K, Kusne AG, Paglione J, Takeuchi I. Artificial intelligence for search and discovery of quantum materials. Commun Mater 2021;2:105. https://doi.org/10.1038/s43246-021-00209-z.
[73] Roeser, H.P., Hetfleisch, Huber, F.M., Stepper, M., von Schoenermark, M.F., Moritz, A., Nikoghosyan, A.S. A link between critical transition temperature and the structure of superconducting $YBa_2Cu_3O_{7-\delta}$. Acta Astronautica 2008, 62, 733–736; doi: https://doi.org/10.1016/j.actaastro.2008.04.004.
[74] Roeser, H.P., Hetfleisch, Huber, F.M., von Schoenermark, M.F., Stepper, M.; Moritz, A., Nikoghosyan, A.S. Correlation between oxygen excess density and critical temperature in superconducting Bi-2201, Bi-2212 and Bi-2223. Acta Astronautica 2008, 63, 1372–1375; doi: 10.1016/j.actaastro.2008.06.001.
[75] Roeser HP, Huber FM, von Schoenermark MF, Nikoghosyan AS. High temperature superconducting with two doping atoms in La-doped Bi-2201 and Y-doped Bi-2212. Acta Astronaut 2009;65:489–94. https://doi.org/10.1016/j.actaastro.2009.02.004.
[76] Roeser HP, Haslam DT, Lopez JS, Stepper M, von Schoenermark MF, Huber FM, Nikoghosyan AS. Electronic energy levels in high-temperature superconductors. J Supercond 2011;24:1443–51. https://doi.org/10.1007/s10948-010-0850-5.
[77] Roeser HP, Bohr A, Haslam DT, López JS, Stepper M, Nikoghosyan AS. Size quantization in high-temperature superconducting cuprates and a link to Einstein's diffusion law. Acta Astronaut 2012;76:37–41. https://doi.org/10.1016/j.actaastro.2012.04.014.
[78] Huber, F.; Roeser, H.P., von Schoenermark, M. A correlation between T_c of Fe-based HT Superconductors and the crystal super lattice constants of the doping element positions. J. Phys. Soc. Jpn. 2008, 77 Suppl. C, 142-144; doi: https://doi.org/10.1143/JPSJS.77SC.142.
[79] Koblischka MR, Roth S, Koblischka-Veneva A, Karwoth T, Wiederhold A, Zeng XL, Fasoulas S, Murakami M. Relation between crystal structure and transition temperature of superconducting metals and alloys. Metals 2020;10:158. https://doi.org/10.3390/met10020158.
[80] Koblischka-Veneva A, Koblischka MR. (RE)BCO and the Roeser-Huber formula. Materials 2021;14:6068. https://doi.org/10.3390/ma14206068.
[81] Koblischka MR, Koblischka-Veneva A. Calculation of T_c of superconducting elements with the Roeser-Huber formalism. Metals 2022;12:337. https://doi.org/10.3390/met1202033Z.
[82] Ghosh KJB, Kais S, Herschbach DR. Dimensional interpolation for metallic hydrogen. Phys Chem Chem Phys 2021;23:7841–8. https://doi.org/10.1039/d0cp05301e.
[83] Mathew S, Abraham Aben Regi, Chintalapati S, Sarkar S, Joseph B, Venkatesan T. Temperature Dependent Structural Evolution of WSe_2: A Synchrotron X-ray Diffraction Study. Condens Matter 2020;5:76. https://doi.org/10.3390/condmat5040076.
[84] Khalaf E, Kruchkov AJ, Tarnopolsky G, Vishwanath A. Magic angle hierarchy in twisted graphene multilayers. Phys Rev B 2019;100:085109. https://doi.org/10.1103/PhysRevB.100.085109.
[85] Talantsev EF. Quantifying the Charge Carrier Interaction in Metallic Twisted Bilayer Graphene Superlattices. Nanomaterials 2021;11:1306. https://doi.org/10.3390/nano11051306.
[86] Cai L, Yu G. Fabrication strategies of twisted bilayer graphenes and their unique properties. Adv Mater 2021;33:2004974. https://doi.org/10.1002/adma.202004974.
[87] Fallahazad B, Hao Y, Lee K, Kim S, Ruoff RS, Tutuc E. Quantum Hall effect in Bernal stacked and twisted bilayer graphene grown on Cu by chemical vapor deposition. Phys Rev B 2012;85:201408. https://doi.org/10.1103/PhysRev.85.201408.
[88] Meng L, Zhang Y, Yan W, Feng L, He L, Dou RF, Nie JC. Single-layer behavior and slow carrier density dynamic of twisted graphene bilayer. Appl Phys Lett 2012;100:091601. https://doi.org/10.1063/1.3691952.
[89] Yoo JH, Bin In J, Bok Park J, Jeon H, Grigoropoulos CP. Graphene folds by femtosecond laser ablation. Appl Phys Lett 2012;100:233124. https://doi.org/10.1063/1.4724213.
[90] Mahapatra PS, Sarkar K, Krishnamurthy HR, Mukerjee S, Ghosh A. Seebeck coefficient of a single van der Waals junction in twisted bilayer graphene. Nano Lett 2017;17:6822–7. https://doi.org/10.1021/acs.nanolett.7b03097.
[91] Meissner W, Ochsenfeld R. Ein neuer Effekt bei Eintritt der Supraleitfähigkeit. Naturwissenschaften 1933;21:787–8.
[92] Buckel W, Supraleitung Kleiner R. Grundlagen und Anwendungen. 7th edition,. Weinheim: Wiley-VCH; 2013.
[93] Garisto D. Replication efforts fail for claimed superconductor LK-99. Nature 2023;620:253. https://doi.org/10.1038/d41586-023-02481-0.
[94] Koblischka MR, Wijngaarden RJ. Magneto-optical investigations of superconductors. Supercond Sci Technol 1995;8:199–213. https://doi.org/10.1088/0953-2048/8/4/002.
[95] Bending SJ. Local magnetic probes of superconductors. Adv Phys 1999;48:449–535. https://doi.org/10.1080/000187399243437.
[96] Koblischka MR, Hartmann U. Recent advances in magnetic force microscopy. Ultramicroscopy 2003;97:103–12. https://doi.org/10.1016/S0304-3991(03)00034-2.
[97] Oral A, Bending SJ, Henini M. Real-time scanning Hall probe microscopy. Appl Phys Lett 1996;69(9):1324–6. https://doi.org/10.1063/1.117582.
[98] Sonusen S, Karci O, Dede M, Aksoy S, Oral A. Single layer graphene Hall sensors for scanning Hall probe microscopy (SHPM) in 3–300 K temperature range. Appl Surf Sci 2014;308:414–8. https://doi.org/10.1016/j.apsusc.2014.04.191.
[99] Anahory Y, Naren HR, Lachman EO, Buhbut Sinai S, Uri A, Embon L, Yaakobi E, Myasoedov Y, Huber ME, Klajn R, Zeldov E. SQUID-on-tip with single-electron spin sensitivity for high-field and ultra-low temperature nanomagnetic imaging. Nanoscale 2020;12:3174. https://doi.org/10.1039/c9nr08578e.
[100] Levine EV, Turner MJ, Kehayias P, Hart CA, Langellier N, Trubko R, Glenn DR, Fu RR, Walsworth RL. Principles and techniques of the quantum diamond microscope. Nanophotonics 2019;8(11):1945–73. https://doi.org/10.1515/nanoph-2019-0209.
[101] Hong S, Grinolds MS, Pham LM, Le Sage D, Luan L, Walsworth RL, Yacoby A. Nanoscale magnetometry with NV centers in diamond. MRS Bull 2013;38:155–61. https://doi.org/10.1557/mrs.2013.23.
[102] Wenzhao Li W, Reichhardt CJO, Jankó B, Reichhardt C. Vortex dynamics, pinning, and angle-dependent motion on moiré patterns. Phys Rev B 2021;104:024504. https://doi.org/10.1103/PhysRevB.104.024504.
[103] Gorter CJ, Casimir H. On supraconductivity I. Physica 1934;1:306–20.
[104] Poole Jr CP, Creswick RJ, Farach HA, Prozorov R. Superconductivity. UK: Elsevier; 2007. Second edition.
[105] Talantsev EF, Crump WP, Island JO, Xing Y, Sun Y, Wang J, Tallon JL. On the origin of critical temperature enhancement in atomically thin superconductors. 2D Materials 2017;4:025072. https://doi.org/10.1088/2053-1583/aa6917.

[106] Pal, B.; Joshi, B P.; Chakraborti, H.; Jain, A.K.; Barick, B.K.; Ghosh, K.; Bhunia, S.; Laha, A.; Dhar, S.; Gupta, Das. K. Experimental evidence of a very thin superconducting layer in epitaxial indium nitride. Supercond. Sci. Technol. 32, 015009; doi: https://doi.org/10.1088/1361-6668/aaed8f.
[107] Helfand E, Werthamer NR. Temperature and purity dependence of the superconducting critical field. H_{c2} II Phys Rev 1966;147:288–94. https://doi.org/10.1103/PhysRev.147.288.
[108] Werthamer NR, Helfand E, Hohenberg PC. Temperature and purity dependence of the superconducting critical field, H_{c2}. III. Electron spin and spin-orbit effects. Phys Rev 1966;147:295–302. https://doi.org/10.1103/PhysRev.147.295.
[109] Baumgartner T, Eisterer M, Weber HW, Flükiger R, Scheuerlein C, Bottura L. Effects of neutron irradiation on pinning force scaling in state-of-the-art Nb_3Sn wires. Supercond Sci Technol 2014;27:015005. https://doi.org/10.1088/0953-2048/27/1/015005.
[110] Jones CK, Hulm JK, Chandrasekhar BS. Upper critical field of solid solution alloys of the transition elements. Rev Mod Phys 1964;1964(36):74–6. https://doi.org/10.1103/RevModPhys.36.74.
[111] Talantsev EF. DC self-field critical current in superconductor/Dirac-cone material/superconductor junctions. Nanomaterials 2019;9:1554. https://doi.org/10.3390/nano9111554.
[112] Schrieffer JR, Scalapino DJ, Wilkins JW. Effective tunneling density of states in superconductors. Phys Rev Lett 1963;10:336–9.
[113] McMillan WL, Rowell JM. Lead phonon spectrum calculated from superconducting density of states. Phys Rev Lett 1965;1965(14):108–12.
[114] Zasadzinski JF, Ozyuzer L, Miyakawa N, Gray KE, Hinks DG, Kendziora C. Correlation of tunneling spectra in $Bi_2Sr_2CaCu_2O_{8+\delta}$ with the resonance spin excitation. Phys Rev Lett 2001;87:067005. https://doi.org/10.1103/PhysRevLett.87.067005.
[115] Lee J, Fujita K, McElroy K, Slezak JA, Wang M, Aiura Y, Bando H, Ishikado M, Masui T, Zhu J-X, Balatsky AV, Eisaki H, Uchida S, Davis JC. Interplay of electron–lattice interactions and superconductivity in $Bi_2Sr_2CaCu_2O_{8+\delta}$. Nature 2006;442:546–50. https://doi.org/10.1038/nature04973.
[116] Niestemski FC, Kunwar S, Zhou S, Li S, Ding H, Wang Z, Dai P, Madhavan V. A distinct bosonic mode in an electron-doped high-transition-temperature superconductor. Nature 2007;450:1058–61. https://doi.org/10.1038/nature06430.
[117] Das P, Koblischka MR, Rosner H, Wolf T, Hartmann U. Excitation of a bosonic mode by electron tunneling into a cuprate superconductor $NdBa_2Cu_3O_{7-\delta}$. Phys Rev B 2008;78:214505. https://doi.org/10.1103/PhysRevB.78.214505.
[118] Chi S, Grothe S, Liang R, Dosanjh P, Hardy WN, Burke SA, Bonn DA, Pennec Y. Scanning tunneling spectroscopy of superconducting LiFeAs single crystals: evidence for two nodeless energy gaps and coupling to a bosonic mode. Phys Rev Lett 2012;109:087002. https://doi.org/10.1103/PhysRevLett.109.087002.
[119] Shan L, Gong J, Wang Y-L, Shen B, Hou X, Ren C, Li C, Yang H, Wen H-H, Li S, Dai P. Evidence of a spin resonance mode in the iron-based superconductor $Ba_{0.6}K_{0.4}Fe_2As_2$ from scanning tunneling spectroscopy. Phys Rev Lett 2012;108:227002. https://doi.org/10.1103/PhysRevLett.108.227002.
[120] Ramires A, Lado JL. Emulating heavy fermions in twisted trilayer graphene. Phys Rev Lett 2021;127:026401. https://doi.org/10.1103/PhysRevLett.127.026401.
[121] Carbotte JP. Properties of boson-exchange superconductors. Rev Mod Phys 1990;62:1027–157. https://doi.org/10.1103/PhysRevLett.62.1027.
[122] Song C-L, Hoffman JE. Pairing insights in iron-based superconductors from scanning tunneling microscopy. Curr Opin Solid State Mater Sci 2013;17:39–48. https://doi.org/10.1016/j.cossms.2013.03.005.
[123] Scalapino DJ, Schrieffer JR, Wilkins JW. Strong-coupling superconductivity. I Phys Rev 1966;148:263–79. https://doi.org/10.1103/PhysRev.148.263.
[124] Koblischka-Veneva A, Koblischka MR. High-T_c Cuprate Superconductors: Materials, Structures and Properties. In: Slimani Y, Hannachi E, editors. Superconducting Materials. Fundamentals, Synthesis and Applications, Chap. 7. Singapore: Springer-Nature; 2022. p. 181–210.
[125] Talantsev EF. Critical de Broglie wavelength in superconductors. Mod Phys Lett B 2018;32:1850114. https://doi.org/10.1142/S0217984918501142.
[126] Rohlf JW. Modern Physics from α to Z^0. New York: Wiley; 1994.
[127] Mori N, Wilson JA, Ozaki H. Fluctuation conductivity in the 110-K phase of Ni-doped (Bi, Pb)-Sr-Ca-Cu-O superconductors. Phys Rev B 1992;45:10633–8. https://doi.org/10.1103/PhysRevB.45.10633.
[128] Larkin A, Varlamov A. Fluctuation Phenomena in Superconductors. Oxford, U. K.: Oxford University Press; 2005.
[129] Koblischka MR, Koblischka-Veneva A, Zeng XL, Hannachi E, Slimani Y. Microstructure and Fluctuation-Induced Conductivity Analysis of $Bi_2Sr_2CaCu_2O_{8+\delta}$ (Bi-2212) Nanowire Fabrics. Crystals 2020;10:986. https://doi.org/10.3390/cryst10110986.
[130] Uemura YJ, Le LP, Luke GM, Sternlieb BJ, Wu WD, Brewer JH, Riseman TM, Seaman CL, Maple MB, Ishikawa M, Hinks DG, Jorgensen JD, Saito G, Yamochi H. Basic Similarities among Cuprate, Bismuthate, Organic, Chevrel-Phase, and Heavy-Fermion Superconductors Shown by Penetration Depth Measurements. Phys Rev Lett 1991;66:2665–8. https://doi.org/10.1103/PhysRevLett.66.2665.
[131] Uemura YJ. Condensation, excitation, pairing, and superfluid density in high-T_c superconductors: the magnetic resonance mode as a roton analogue and a possible spin-mediated pairing. J Phys: Condens Matter 2004,;16:S4515–40. https://doi.org/10.1088/0953-8984/16/40/007.
[132] Harshman DR, Fiory AT. High-T_c Superconductivity Originating from Interlayer Coulomb Coupling in Gate-Charged Twisted Bilayer Graphene Moiré Superlattices. J Supercond Novel Magn 2020;33:367–78. https://doi.org/10.1007/s10948-019-05183-9.
[133] Xiao Y, Liu J, Fu L. Moiré is more: access to new properties of two-dimensional layered materials. Matter 2020;3:1142–61. https://doi.org/10.1016/j.matt.2020.07.001.
[134] Boochani A, Jamal M, Shahrokhi M, Nowrozi B, Gholivand MB, Khodadadi J, Amiri M, Asshabia M, Yaria A. Ti_2VGe Heuslerene: theoretical prediction of a novel 2D material. J Mater Chem C 2019;7:13559. https://doi.org/10.1039/c9tc03176f.
[135] Wang T, Noah F, Yuan Q, Fu L. Moiré surface states and enhanced superconductivity in topological insulators. Phys Rev X 2021;11:021024. https://doi.org/10.1103/PhysRevX.11.021024.
[136] Kezilebieke S, Vano V, Huda MdN, Aapro M, Ganguli SC, Liljeroth P, Lado JL. Moiré-enabled topological superconductivity. Nano Lett 2022;22:328–33. https://doi.org/10.1021/acs.nanolett.1c03856.
[137] Carr S, Massatt D, Fang S, Cazeaux P, Luskin M, Kaxiras E. Twistronics: manipulating the electronic properties of two-dimensional layered structures through their twist angle. Phys Rev B 2017;95:075420. https://doi.org/10.1103/PhysRevB.95.075420.